Intrinsic Nonlinearity and Spectral Structure of Internal Tides at an Idealized Mid-Atlantic Bight Shelf Break

WEIFENG G. ZHANG AND TIMOTHY F. DUDA

Applied Ocean Physics and Engineering Department, Woods Hole Oceanographic Institution, Woods Hole, Massachusetts

(Manuscript received 10 December 2012, in final form 28 August 2013)

ABSTRACT

To quantify dynamical aspects of internal-tide generation at the Mid-Atlantic Bight shelf break, this study employs an idealized ocean model initialized by climatological summertime stratification and forced by monochromatic barotropic tidal currents at the offshore boundary. The Froude number of the scenario is subunity, and the bathymetric slope offshore of the shelf break is supercritical. A barotropic-to-baroclinic energy conversion rate of 335 W m^{-1} is found, with 14% of the energy locally dissipated through turbulence and bottom friction and 18% radiated onto the shelf. Consistent with prior studies, nonlinear effects result in additional super- and subharmonic internal waves at the shelf break. The subharmonic waves are subinertial, evanescent, and mostly trapped within a narrow beam of internal waves at the forcing frequency. They likely result from nonresonant triad interaction associated with strong nonlinearity. Strong vertical shear associated with the subharmonic waves tends to enhance local energy dissipation and turbulent momentum exchange (TME). A simulation with reduced tidal forcing shows an expected diminished level of harmonic energy. A quasi-linear simulation verifies the role of momentum advection in controlling the relative phases of internal tides and the efficiency of barotropic-to-baroclinic energy conversion. The local TME is tightly coupled with the internal-wave dynamics: for the chosen configuration, neglecting TME causes the internal-wave energy to be overestimated by 12%, and increasing it to high levels damps the waves on the continental shelf. This work implies a necessity to carefully consider nonlinearity and turbulent processes in the calculation of internal tidal waves generated at the shelf break.

1. Introduction

Internal waves generated at continental shelf edges can be dissipated within a few tens of kilometers, influencing local stratification (Holloway et al. 2001; Klymak et al. 2010; Levine and Boyd 2006), or be transported on- or offshore. Onshore propagation of the waves into water of decreasing depth raises their energy density, possibly leading to short nonlinear waves with nonhydrostatic pressure (Apel et al. 1997; Sandstrom and Elliott 1984) and strong dissipation over a distance of 50 km or greater (Shroyer et al. 2010a). Here, generation of internal tides (tidal frequency internal waves) at an idealized Mid-Atlantic Bight (MAB) shelf break by barotropic tides is examined (Fig. 1). The practical motivation for the study is a desire to define a prediction capability for nonlinear internal waves on the shelf. These waves can have large acoustical effects (Lynch et al. 2010), and the possibility of predicting their locations, directions, sizes, shapes, and other characteristics is being examined. This is a challenging problem, as illustrated in a recent paper suggesting that internal waves incident on the continental slope, potentially unknowable, may at times play a significant role (Nash et al. 2012). Despite this, it is likely that internal tides generated at the shelf edge can be important precursors to nonlinear wave packets on the shelf, and we wish to determine the prediction capability, while recognizing the inherent impossibility of the complete prediction of nonlinear phenomena (Eckmann and Ruelle 1985; Krishnamurthy 1993).

A number of geometric factors control the characteristics of the internal waves at a shelf edge, including particle excursion, topography scale length, and steepness of slope (Garrett and Kunze 2007). Because the geometry and the stratification can vary so broadly,

Corresponding author address: Weifeng G. Zhang, Applied Ocean Physics and Engineering Department, Woods Hole Oceanographic Institution, 266 Woods Hole Road, Woods Hole, MA 02543.
E-mail: wzhang@whoi.edu

DOI: 10.1175/JPO-D-12-0239.1

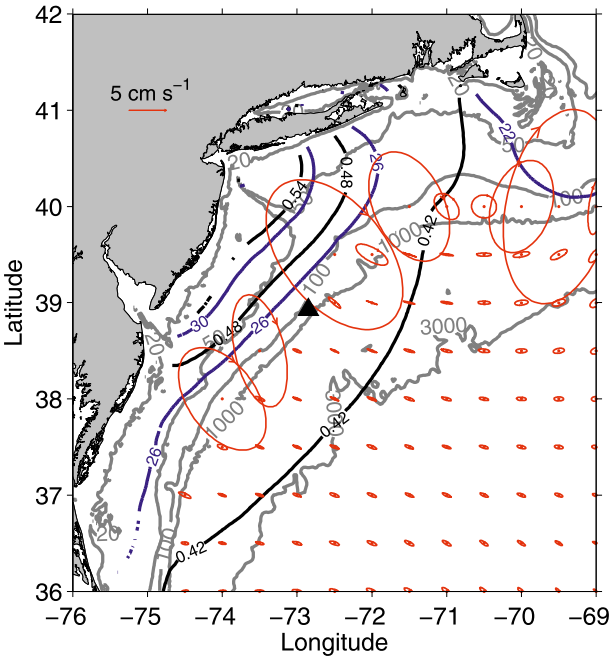

FIG. 1. Bathymetry and properties of barotropic M_2 tide in the MAB area. Gray lines are bathymetric contours (m), black solid lines are M_2 tidal elevation contours (m), blue dashed lines are M_2 tidal phase contours (°), red ellipses are M_2 tidal ellipses at selected locations (the scale on land is for major and minor axes of the tidal ellipses), and the black triangle indicates the location of the Shallow Water '06 Mooring SW43.

computational models are often used to determine the effects (e.g., Gerkema et al. 2006; Green et al. 2008; Holloway and Barnes 1998; Legg and Adcroft 2003). However, questions remain, including which modeling techniques are best, which are adequate, and what errors are introduced by specific modeling procedures. This study also employs a computational flow model and tries to answer some of the modeling questions. A primitive equation hydrostatic model is used to study the low-frequency (with periods longer than 2 h) internal waves generated locally by the barotropic principal lunar semidiurnal M_2 tide at the idealized shelf break.

The internal-wave fields resulting from our simulations are formed by only one of the processes responsible for ocean internal waves. This paper addresses two mechanisms at work in the energy balance of tidally driven internal waves in their generation region: nonlinear boundary zone effects and nonlinear wave–wave interaction. Both of these affect the level and shape of the resultant internal wave–frequency spectrum. The questions addressed here are as follows: 1) What fraction of internal-wave energy provided by tidal processes resides in the tidal frequencies, and what fraction in other frequencies? 2) How important is nonlinear momentum advection in the generation region? 3) How does imposed subgrid turbulent momentum exchange (TME) affect the internal-tide generation?

Resonant nonlinear wave–wave interaction (McComas and Bretherton 1977; Müller et al. 1986) is a potential mechanism of filling the internal wave–frequency band, from inertial frequency f to buoyancy frequency N, with energy moving from waves at a few source wavenumbers $\mathbf{k}$ and frequencies ω (i.e., near inertial and tidal) to other $\mathbf{k}$ and ω, with net flux to waves that dissipate. Parametric subharmonic instability (PSI), one of the many types of resonant interactions, generates waves of a frequency near one-half of the forcing frequency and high vertical wavenumbers, and can therefore potentially induce strong TME, especially near the critical latitude (Gerkema et al. 2006; Lamb 2004; MacKinnon and Winters 2005; Young et al. 2008). Therefore, a better understanding of nonlinear wave–wave interactions would be an important step toward full knowledge of the wave field itself, from the generation processes to the physical–biogeochemical impacts of wave dissipation. Nonlinear wave–wave interaction has been demonstrated a few times in the field (Carter and Gregg 2006; MacKinnon et al. 2013; Sun and Pinkel 2012, 2013) and numerous times in models (e.g., Hazewinkel and Winters 2011; Korobov and Lamb 2008; Legg and Huijts 2006; Nikurashin and Legg 2011), and it has been shown to enhance turbulence dissipation in the open ocean environment (Lvov et al. 2012; Nikurashin and Legg 2011; Polzin 2004a,b; Winters and D'Asaro 1997).

In addition to demonstrating the development of expected fundamental internal waves and superharmonic waves (via nonlinear resonant wave–wave interactions), this three-dimensional study examines subinertial evanescent waves appearing trapped in an internal-tide beam. A study by Korobov and Lamb (2008) examined the generation of subinertial, trapped waves using two-dimensional numerical simulations and attributed the phenomenon to nonlinear nonresonant interaction of internal waves. Their findings echo observations of standing evanescent waves at frequencies greater than N in the intersections of two internal-wave beams in both laboratory (Teoh et al. 1997) and numerical (Javam et al. 1999, 2000) settings. Here, the transfer of internal-wave energy from the primary frequency to other (sub and super) harmonics is quantified for the chosen shelfbreak environment.

Substantial internal-wave activities have been observed in the MAB shelfbreak region (Nash et al. 2004; Shroyer et al. 2011; Tang et al. 2007) and may dominate local TME and tracer mixing (MacKinnon and Gregg 2005; Shroyer et al. 2010b). The M_2 is the dominant tidal constituent in the area, and the M_2 tide propagates

mainly toward the coast (Fig. 1). The barotropic tidal current speed increases dramatically across the shelf break, from about 1.5 cm s^{-1} at the 1000-m isobath to about 10 cm s^{-1} at the 100-m isobath. In this study, we neglect influences of factors on the internal-tide generation, such as other tidal constituents, mesoscale activities, meteorological forcing, bathymetric irregularity, and internal waves radiating into the area (Nash et al. 2012). Barotropic-to-baroclinic energy conversion at the shelfbreak region under a climatological summer condition is quantified, and influences of nonlinear momentum advection and TME on the conversion are investigated. The model setup represents a highly idealized single scenario, and the results achieved here provide only an instructive example of the dynamics presumably associated with internal-tide generation over a broader range of scenarios than can be examined in one paper.

2. Experiment setup

a. Basic model configuration

The hydrostatic Regional Ocean Modeling System (ROMS), with terrain-following vertical coordinates, is used for the simulations (http://www.myroms.org; Shchepetkin and McWilliams 2005, 2008). Using the hydrostatic pressure approximation in the model is justifiable because internal tides generated at the shelf break are of low frequency, and the associated vertical accelerations (a major component of the nonhydrostatic pressure) are small. As these waves propagate in nature onto the shallow shelf they evolve into bores and short nonlinear internal waves [O(100 m)], which are not properly handled by the hydrostatic model. Therefore, details in that regime are not examined here.

The positive x direction is offshore and southeastward (to mimic MAB), positive y is northeastward, and positive z is upward with $z = 0$ at the sea surface. With the hydrostatic pressure assumption, the model solves the horizontal momentum equation

$$\frac{\partial \mathbf{u}_h}{\partial t} + \mathbf{u}\cdot\nabla\mathbf{u}_h + \mathbf{f}\times\mathbf{u}_h = -\frac{1}{\rho_0}\nabla_h p + \frac{1}{\rho_0}\frac{\partial}{\partial z}\left(A_v\frac{\partial \mathbf{u}_h}{\partial z}\right), \tag{1}$$

the continuity equation

$$\nabla\cdot\mathbf{u} = 0, \tag{2}$$

scalar equations for temperature T and salinity S, and the nonlinear equation of state. Here, $\mathbf{u}$ is three-dimensional velocity vector (u, v, w), $\mathbf{u}_h$ is horizontal velocity vector $(u, v, 0)$, $\mathbf{f}$ is the Coriolis vector $(0, 0, f)$,

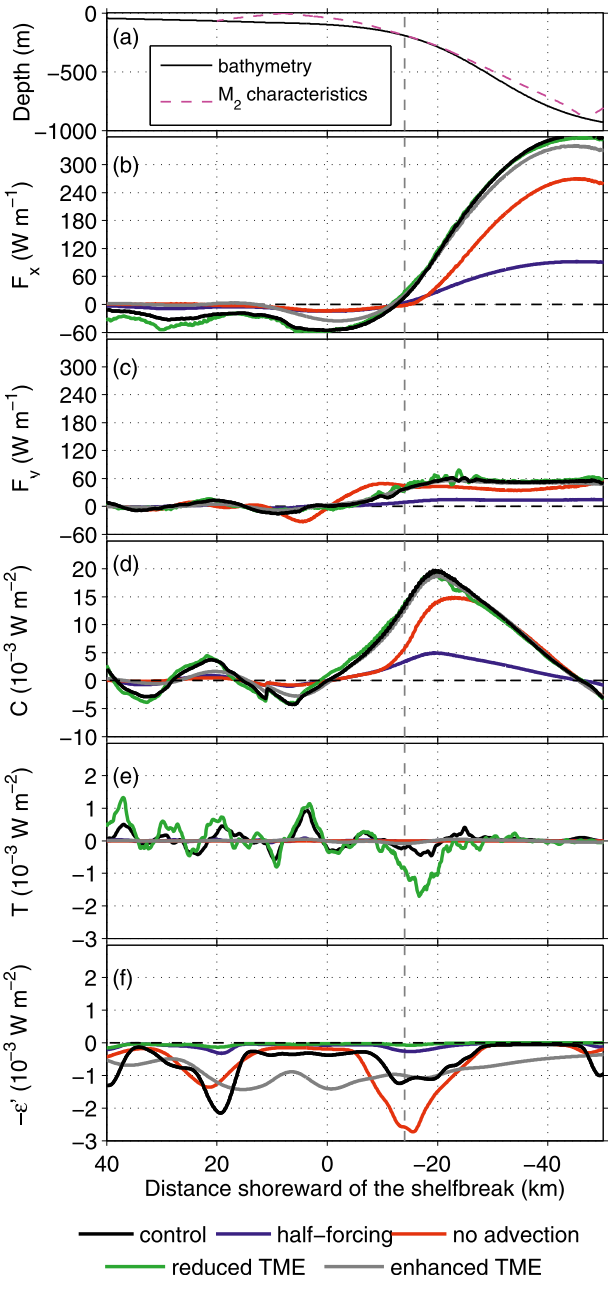

FIG. 2. For the five simulations: (a) central part of the model bathymetry and M_2 internal-wave characteristics (magenta lines); vertically integrated (b) cross- and (c) along-shelf baroclinic energy fluxes; (d) barotropic-to-baroclinic energy conversion rate; (e) total advection of baroclinic energy; and (f) turbulence dissipation rate. The gray dashed line indicates the site of critical slope.

ρ_0 is reference density, p is pressure, and A_v is the TME coefficient (vertical eddy viscosity) acting on vertical shear. Model bathymetry is uniform in the along-shelf direction, and its cross-shelf form (Fig. 2a) is given by

$$H = \max[0, \alpha(x_1 - x)] + h_0\tanh\left(\frac{x_0 - x}{L}\right) - h_1, \tag{3}$$

where $\alpha = 0.001$, $x_1 = 64$ km, $x_0 = 105$ km, $L = 16.5$ km, $h_0 = 465$ m, and $h_1 = 540$ m. This function of x has a uniform slope α on the shelf transitioning to a hyperbolic tangent shape in the slope sea. Values of the parameters are chosen to represent the mean slope of the MAB continental shelf, to fit the along-shelf-averaged MAB shelfbreak bathymetry (water depth of 100–400 m), and to limit the maximum depth at 1000 m. Limiting the maximum depth maintains the model's vertical resolution in the deep sea.

The model domain spans an area of 1931 km (x direction) × 27 km (y direction). The nearshore 150 km in the x direction is the study area. The horizontal resolution in the study area is 121 and 149 m in the x and y directions, respectively. The region outside the study area is to delay the reflection of internal waves at the offshore boundary; its y resolution is 149 m and its x resolution coarsens gradually from 121 m to 6.2 km toward the offshore boundary. There are 100 stretched vertical layers with enhanced resolution near the surface and bottom (about 0.2 m at the shelf break). The Coriolis parameter $f = 2\Omega \sin(39°)$, where Ω is the earth's rotation rate.

The coastal boundary is a solid wall with depth of 10 m. Periodic boundary conditions are used in the y direction. The deep-sea boundary is open with the Chapman (1985), Flather (1976), and Orlanski-type radiation (Orlanski 1976) conditions used for sea level, two-dimensional momentum, and three-dimensional variables, respectively. In the control simulation, barotropic tidal velocity of only the principal lunar M_2 frequency is added on the offshore boundary, adjusted to generate a deep-sea current ellipse with major axis of $0.02\ \mathrm{m\,s^{-1}}$ and inclination pointing onshore, consistent with the averaged properties at 1000-m isobath in the MAB retrieved from the Oregon State University (OSU) Tidal Inversion Software (OTIS) regional tidal solution (http://volkov.oce.orst.edu/tides/region.html). The resultant barotropic tidal current at the shelf break (100-m isobath) has amplitude of $0.12\ \mathrm{m\,s^{-1}}$ in the cross-shelf direction, the same value as OTIS (Fig. 1), with this consistency justifying the limited depth of 1000 m. A 600-km-wide sponge layer is applied at the offshore end of the domain (outside of the study area) to further prevent reflection of internal waves at the offshore boundary. No explicit horizontal viscosity or diffusivity is applied in the interior. The numerical advection schemes are third-order upstream bias and fourth-order centered for three-dimensional horizontal and vertical momentum advection, respectively, and fourth-order Akima for both horizontal and vertical tracer advection.

The control simulation employs the generic length scale (GLS) turbulence closure K–KL scheme (Umlauf and Burchard 2003; Warner et al. 2005) for the vertical TME and tracer mixing. The turbulence closure model solves two dynamical equations (one for turbulence kinetic energy K and the other for KL, where L is the turbulent length scale) derived from transport of the Reynolds stress tensor. Typically, the resulting vertical eddy viscosity and diffusivity κ_v are on the order of $10^{-3}\ \mathrm{m^2\,s^{-1}}$ in the bottom boundary layer (BBL; about 5 m near the bottom) and gradually reduce to $10^{-4}\ \mathrm{m^2\,s^{-1}}$ in the interior and then $10^{-5}\ \mathrm{m^2\,s^{-1}}$ in the thermocline. The Prandtl number (A_v/κ_v) is about 1 in the BBL and 1.5 in the thermocline. Note that A_v and κ_v are derived separately from K and L using different quasi-equilibrium stability functions (Kantha and Clayson 1994).

All model simulations start from rest with a horizontally uniform density structure (Fig. 3) obtained from summertime T and S climatology in the region (Zhang et al. 2011). Quadratic bottom drag is used with a drag coefficient $C_d = 0.003$. The model has no heat, salt, or momentum exchange with the atmosphere. All simulations last for 25 days; within the first 10 days, internal waves with a period greater than 2 h are well developed (see below). We therefore chose day 10 (two M_2 periods) as the time window to analyze characteristics of modeled internal-tide fields. For the time series analyses, we selected two sites, A and B (Fig. 4a). Site A, 145 m below the surface, is within the M_2 beam and slightly above the critical slope. Site B, 37 m below the surface, is about 10 km onshore of the shelf break and slightly below a surface-reflected M_2 internal-tidal beam (see section 3a).

b. Equations of baroclinic motion

Under the assumption that the flow can be decomposed into barotropic and baroclinic components, we write

$$\mathbf{u} = \mathbf{U} + \mathbf{u}' \quad \text{and} \quad p = P + p', \tag{4}$$

where $\mathbf{U} = \int_{-H}^{0} \mathbf{u}\, dz$ is barotropic velocity, P is barotropic pressure, $\mathbf{u}'$ is baroclinic velocity, and p' is perturbation pressure. Subtracting the equation of barotropic flow (with no TME) from (1) gives the horizontal baroclinic momentum equation:

$$\frac{\partial \mathbf{u}_h'}{\partial t} + \mathbf{U}\cdot\nabla\mathbf{u}_h' + \mathbf{u}'\cdot\nabla\mathbf{U}_h + \mathbf{u}'\cdot\nabla\mathbf{u}_h' + \mathbf{f}\times\mathbf{u}_h' = -\frac{1}{\rho_0}\nabla_h p' + \mathbf{M}. \tag{5}$$

Here, $\mathbf{M}$ is the eddy viscosity term that contains both barotropic and baroclinic flows. Note that the nonlinear momentum advection term in (1), $\mathbf{u}\cdot\nabla\mathbf{u}_h$, breaks into four parts, three of which appear in (5). Among them, $\mathbf{U}\cdot\nabla\mathbf{u}_h'$ and $\mathbf{u}'\cdot\nabla\mathbf{u}_h'$ represent barotropic and baroclinic

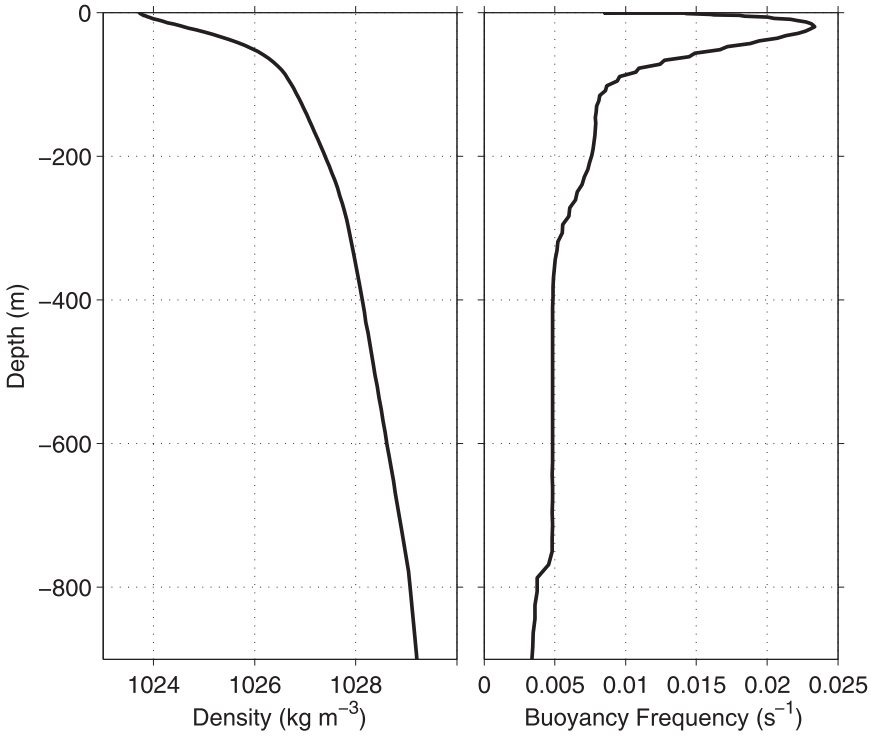

FIG. 3. Summertime climatological vertical profiles of (left) density and (right) buoyancy frequency in the MAB that are used to initialize the model.

advection of the baroclinic momentum, respectively. We refer to $\mathbf{U}\cdot\nabla\mathbf{u}_h'$ as ''baroclinically linear'' and $\mathbf{u}'\cdot\nabla\mathbf{u}_h'$ as ''baroclinically nonlinear'' processes. The term $\mathbf{u}'\cdot\nabla\mathbf{U}_h$ is also ''baroclinically linear,'' but negligible because $\mathbf{U}$ has a small wavenumber. The equation for baroclinic flow kinetic energy averaged over a tidal period is

$$\frac{\partial E_{kz}}{\partial t} = C_z + T_z - \nabla\cdot\mathbf{F}_z - \varepsilon_z' - D'. \tag{6}$$

The terms and additional quantities are defined as follows. The period-averaged internal-wave kinetic energy is

$$E_{kz} = \frac{1}{2}\rho_0\langle\mathbf{u}'\cdot\mathbf{u}'\rangle; \tag{7}$$

the barotropic-to-baroclinic energy conversion rate is

$$C_z(x,z) = \langle\rho' g W_z\rangle; \tag{8}$$

the advection of baroclinic kinetic energy is

$$T_z = -\rho_0\langle\mathbf{u}_h'\cdot(\mathbf{U}\cdot\nabla\mathbf{u}_h')\rangle - \rho_0\langle\mathbf{u}_h'\cdot(\mathbf{u}'\cdot\nabla\mathbf{U}_h)\rangle - \rho_0\langle\mathbf{u}_h'\cdot(\mathbf{u}'\cdot\nabla\mathbf{u}_h')\rangle; \tag{9}$$

the baroclinic energy flux vector is

$$\mathbf{F}_z = (F_{xz}, F_{yz}, F_{wz}) = \langle\mathbf{u}'p'\rangle; \tag{10}$$

the interior dissipation rate is (Kang and Fringer 2012)

$$\varepsilon_z' \approx \left\langle \rho_0 A_v \frac{d\mathbf{u}'}{dz}\cdot\frac{d\mathbf{u}'}{dz} + g\kappa_v\frac{\partial\rho}{\partial z}\frac{\partial\zeta}{\partial z}\right\rangle; \tag{11}$$

the dissipation due to bottom friction is (Kang and Fringer 2012)

$$D' = \rho_0 C_d|\mathbf{u}_b|(\mathbf{u}_b\cdot\mathbf{u}_b'); \quad \text{and} \tag{12}$$

and the vertical velocity associated with the barotropic flow is

$$W_z = -\dot{\nabla}[(z+H)\mathbf{U}]. \tag{13}$$

Here, ρ' is perturbation density and ζ is vertical isopycnal displacement. The angle brackets in (7)–(12) indicate a time average over an M_2 wave period. Because advection of available potential energy in this study is at least one order of magnitude smaller than the other terms, it is neglected in energy budget analyses.

c. List of model runs and parameter scalings

To investigate the influences of nonlinear momentum advection and vertical TME on the internal-tide

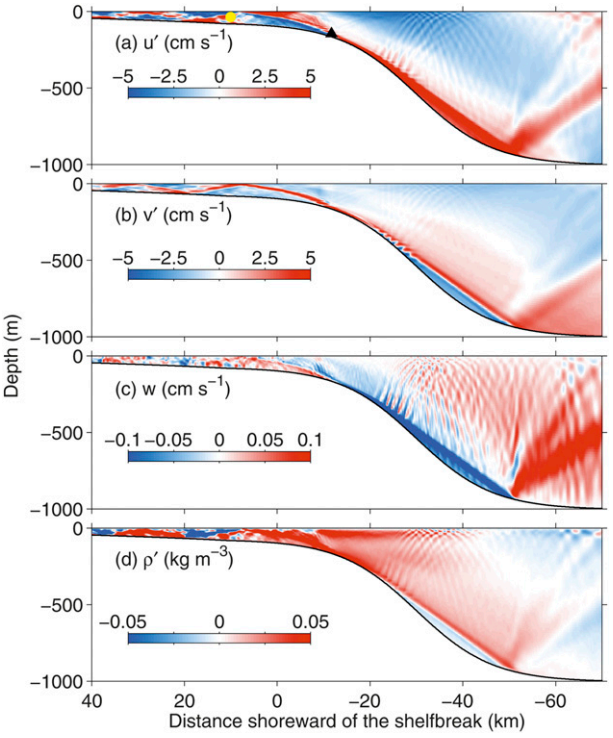

FIG. 4. Snapshots of (a) cross- and (b) along-shelf baroclinic velocity, (c) vertical velocity, and (d) density anomaly in the control simulation at day 10. The black triangle and yellow circle in (a) indicate the locations of sites A and B, respectively.

generation, five runs were conducted as shown in Table 1. The ''control run'' is intended to be the most realistic simulation, while the other sensitivity runs with altered physics serve to illustrate the roles of specific effects. The half-forcing and no-advection runs are to examine the role, in the internal wave–generation process, of nonlinearity (largely caused by $\mathbf{u}\cdot\nabla\mathbf{u}_h$ but also arising from the equation of state and from TME). The reduced and enhanced TME simulations serve to demonstrate the effect of vertical TME.

Several nondimensional parameters are important for the problem of internal-wave generation (Legg and Huijts 2006). Their values for the simulations are given here to provide context for interpreting the model results. The first parameter is the relative topographic height

$$\delta = \frac{h_0}{H_d}, \tag{14}$$

where h_0 is the topographic height, defined here as the depth change across the continental slope, and H_d is the bottom depth of the deep sea. In this study, as $h_0 \approx 900\,\mathrm{m}$ and $H_d = 1000\,\mathrm{m}$, $\delta \approx 0.9$, indicating that the topographic variation is drastic and strong baroclinic responses to barotropic tidal flow are expected. Note that δ is even closer to 1 at the real MAB shelf break. The next parameter is the tidal excursion parameter

$$R = \frac{U_0}{(\omega L)}. \tag{15}$$

This is the ratio of the excursion length at frequency ω, U_0/ω, to the characteristic horizontal length scale L of the local topography (Legg and Klymak 2008; Rayson et al. 2011). Here, U_0 is the characteristic tidal current speed in the shelfbreak region. Because $L \approx 20\,\mathrm{km}$ (Fig. 2a) and $U_0 \approx 0.1\,\mathrm{m\,s^{-1}}$ at the shelf break, $R = U_0/(\omega_{M_2} L) \approx 0.0053$ in this work, suggesting that low-frequency internal tides, instead of high-frequency lee waves, are likely to be generated at the topography.

The third parameter is the normalized seabed slope

$$\gamma = \frac{s}{\alpha}, \tag{16}$$

which is related to the intensity of the internal-wave generation, with the intensity increasing with γ for fixed topographic height. Here, s is the seabed slope, while α is the slope of the (depth dependent) internal wave–energy propagation characteristic satisfying

$$\alpha(z) = \tan\theta = \left[\frac{\omega^2 - f^2}{N(z)^2 - \omega^2}\right]^{1/2} = \frac{k_x}{k_z}. \tag{17}$$

TABLE 1. Simulation list.

Index	Description	Nonlinear momentum advection ($\mathbf{u}\cdot\nabla\mathbf{u}_h$)	Tidal amplitude in the deep sea ($\mathrm{m\,s^{-1}}$)	TME coefficient (i.e., A_v)	Turbulent diffusivity coefficient (i.e., κ_v)
1	Control run	On	0.02	Computed with GLS *K–KL* scheme	Computed with GLS *K–KL* scheme
2	Half-forcing	On	0.01	Computed with GLS *K–KL* scheme	Computed with GLS *K–KL* scheme
3	Quasi-linear run (no advection)	Off	0.02	Computed with GLS *K–KL* scheme	Computed with GLS *K–KL* scheme
4	Reduced TME	On	0.02	$10^{-6}\,\mathrm{m^2\,s^{-1}}$	$10^{-6}\,\mathrm{m^2\,s^{-1}}$
5	Enhanced TME	On	0.02	$10^{-2}\,\mathrm{m^2\,s^{-1}}$	$10^{-6}\,\mathrm{m^2\,s^{-1}}$

In (17), θ is the angle with respect to horizontal, $N(z)$ is the local buoyancy frequency, and k_x is the wavenumber in x direction. Here, α is evaluated at the seabed. In this study, $\gamma = s/\alpha_{M_2} > 1$ (supercritical) for the M_2 tide in the steepest region, while $\gamma < 1$ on the shelf and in the deep sea (Fig. 2a). The shallow critical seabed location ($\gamma = 1$) for M_2 frequency is at about 13 km off the shelf break where bottom depth is 220 m and bottom slope is 0.0138, and intensive generation of internal tides is expected there. Stratification and internal-tide generation are small at the deep critical location. The final parameter is the topographic Froude number

$$\mathrm{Fr} = \frac{U_0}{(h_0 N)}, \tag{18}$$

measuring the influence of stratification and topography on tidal flow (Garrett and Kunze 2007; Legg and Klymak 2008). Here, $N > 0.004\,\mathrm{s}^{-1}$ (Fig. 3b) gives $\mathrm{Fr} < 0.03 \ll 1$, meaning that the stratification and/or topography of the region exert strong influence on the tidal flow, and also that mode-1 internal-wave speed far exceeds U_0.

3. Results

a. Control run

All of the simulations show generation of internal waves at the shelf break, similar to many prior studies of this type (e.g., Gerkema et al. 2006; Lamb 2004; Legg 2004; Nash et al. 2012). Figure 4 shows cross-shelf transects of control-run u', v', w, and ρ' at the time of peak onshore barotropic current at day 10. All panels show beams of M_2-frequency internal waves emitted from the critical slope and reflected at the sea surface and bottom. The vertically integrated baroclinic energy fluxes, $F_x = \int_{-H}^{0} F_{xz}\,dz$ and $F_y = \int_{-H}^{0} F_{yz}\,dz$, (Figs. 2b,c) show that baroclinic energy is generated in the region surrounding the critical slope site and propagates both on- and offshore, with more flux offshore. Peak offshore F_x of $360\,\mathrm{W\,m^{-1}}$ occurs 45 km offshore of the shelf break (Fig. 2b), and peak onshore F_x of about $60\,\mathrm{W\,m^{-1}}$ occurs right at the shelf break. The vertically integrated internal-wave kinetic energy $E_k = \int_{-H}^{0} E_{kz}\,dz$ shows a broad peak around 40 km offshore of the shelf break and drops gradually toward the coast on the shelf (Fig. 5a).

To examine the energy budget and determine the roles of conversion, advection, flux divergence, and dissipation, we computed the right-hand-side terms in (6) over day 10 when E_{kz} has reached its quasi-equilibrium state.

1) A cross-shelf section of C_z/ρ_0 (Fig. 6a) shows peak values along the M_2 beam and maximum conversion near the critical site where the vertically integrated conversion rate $C = \int_{-H}^{0} C_z\,dz$ reaches a peak of $0.02\,\mathrm{W\,m^{-2}}$ (Fig. 2d). Here, C decreases to zero at the shelf break and also 45 km offshore of that, and becomes negative further away from the shelf break (indicating an energy transfer from baroclinic to barotropic flow). The cross-shelf-integrated C between

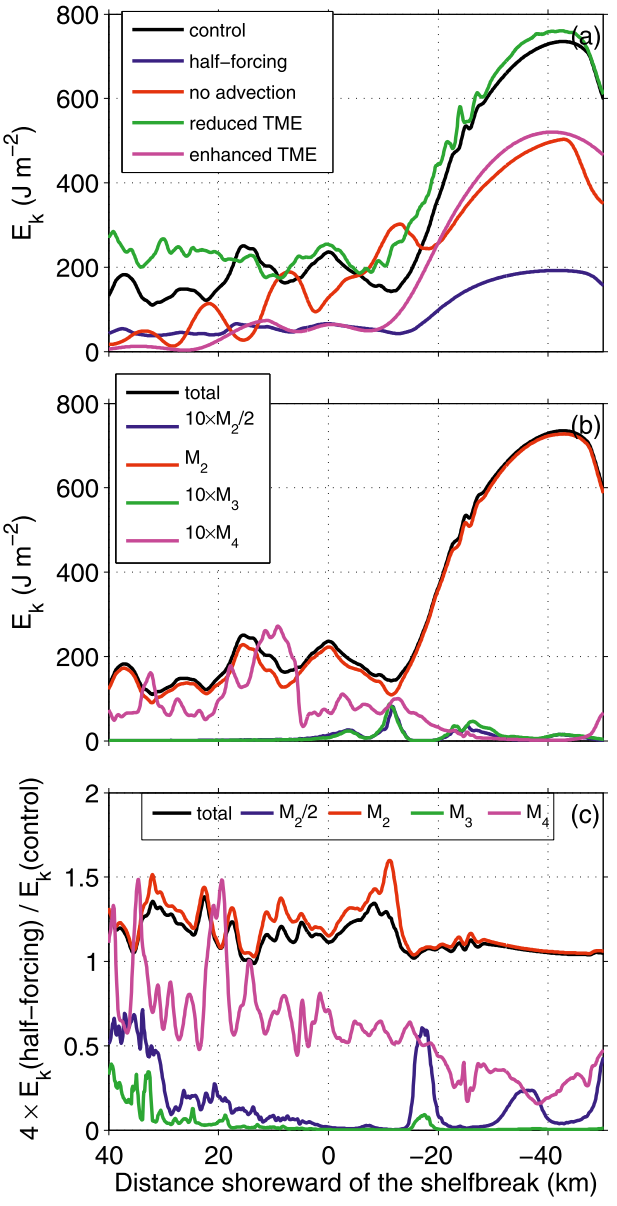

FIG. 5. Cross-shelf distributions of vertically integrated internal wave kinetic energy (a) from simulations of different physics and (b) of waves at different frequencies in the control simulation; and (c) ratios of kinetic energy of waves at different frequencies in the half-forcing simulation to those in the control simulation. The energy of waves at $M_2/2$, M_3, and M_4 frequencies in (b) has been enlarged by 10 times, and ratios in (c) have been multiplied by 4.

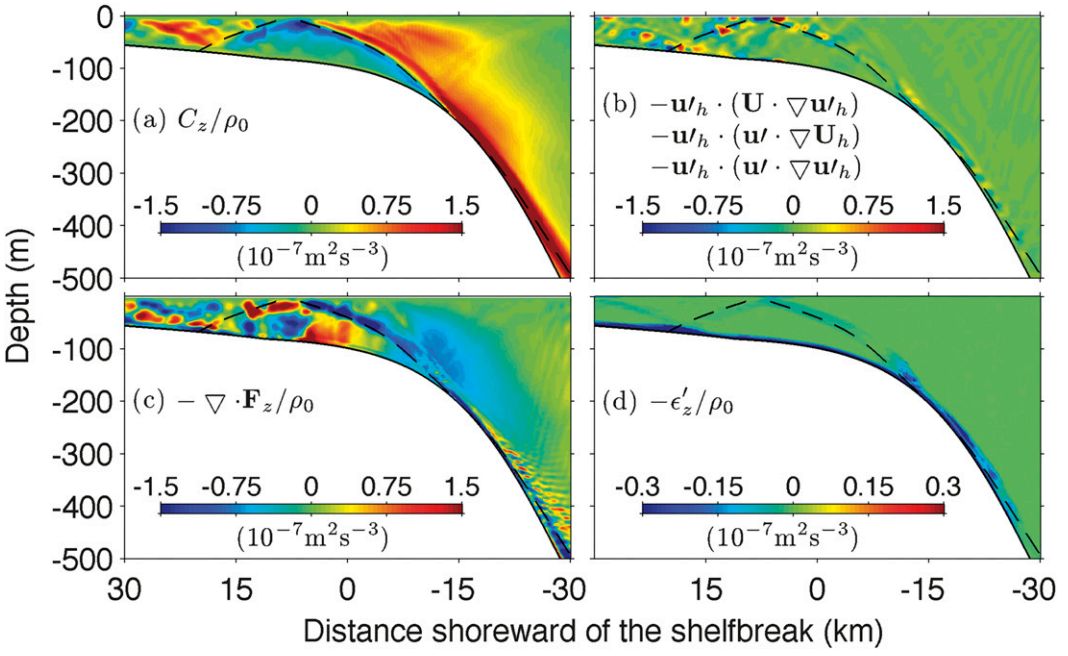

FIG. 6. Cross-shelf section of the rhs terms in the internal wave kinetic energy equation [(6)] over day 10 from the control simulation. The black dashed lines are M_2 internal-wave characteristics.

30 km on- and offshore of the shelf break is about 335 W m^{-1} (Table 2)—slightly smaller than the maximum coherent (presumably locally generated) conversion rate of 400 W m^{-1} estimated from three moorings across the MAB shelf break [Fig. 10e in Nash et al. (2012)]. In Fig. 6a, there is a minor peak of C_z/ρ_0 at 30 m below surface near the shelf break, corresponding to relatively large ρ' at the thermocline depth (Fig. 4d).

2) The flux divergence (Fig. 6c) is large on the shelf and along the M_2 beam offshore of the shelf break, and it is distributed in organized patches of large positive and negative values. Integrated over the area 60 km across the shelf break, $-\nabla \cdot \mathbf{F}_z$ is −295 W m^{-1} (Table 2), making flux divergence the largest sink term for kinetic energy density.
3) Advection of energy (Fig. 6b) is small but present at the shelf break, primarily along the M_2 beam and slightly stronger on the shelf with a patchy distribution. Vertically integrated total advection $T = \int_{-H}^{0} T_z \, dz$ is small and fluctuates, especially on the shelf (Fig. 2e), and T integrated over the area of 60 km across the shelf break is negligible compared to the other terms (Table 2). Figure 7 shows that all terms in (9) are small and, therefore, small T is not caused by cancellation of the terms. Among the terms in (9), $-\langle \mathbf{u}\prime_h \cdot (\mathbf{u}' \cdot \nabla \mathbf{u}\prime_h) \rangle$ is the largest, meaning that the baroclinic self-advection is the dominant advection process.
4) Energy dissipation (Fig. 6d) occurs mostly at the two locations where M_2 beams interact with the seabed: near the critical site and 20 km onshore of the shelf break and vertically integrated dissipation $\varepsilon' = \int_{-H}^{0} \varepsilon'_z \, dz$ reaches peak values at those locations (Fig. 2f). The terms ε' and D' integrated over the area 60 km across the shelf break are 41.8 and 4.6 W m^{-1}, respectively, together equaling about 14% of C in the region (Table 2). Note that the along-beam

TABLE 2. Budget of internal-tide kinetic energy averaged over an area between 30 km on- and offshore of the shelf break.

Index	Description	E_k ($\times 10^5$ J m^{-1})	C (W m^{-1})	T (W m^{-1})	$-\nabla \cdot \mathbf{F}_z$ (W m^{-1})	$-\varepsilon'$ (W m^{-1})	$-D'$ (W m^{-1})
1	Control run	146	335	0.342	−295	−41.8	−4.60
2	Half-forcing	41.2	84.6	0.0632	−76	−6.71	−1.18
3	Quasi-linear run (no advection)	107	223	0	−166	−51.7	−3.43
4	Reduced TME	174	341	−5.87	−320	−2.60	−0.440
5	Enhanced TME	68.6	317	−0.287	−251	−62.1	−0.916

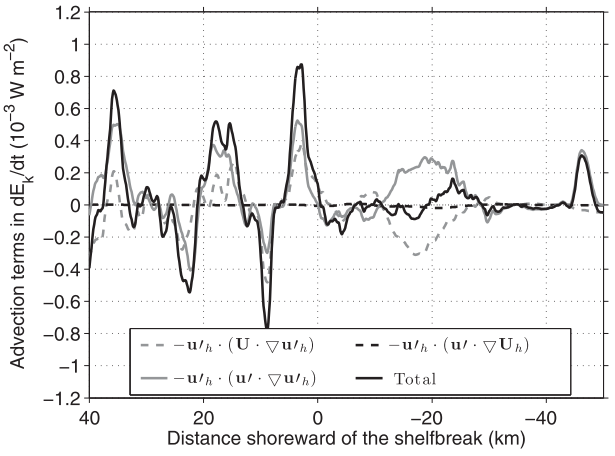

FIG. 7. Vertically integrated advection terms in the internal wave kinetic energy equation [(6)] over day 10 from the control simulation.

patchy patterns in Figs. 6b–6d around 20 km offshore the shelf break resembles that of the subharmonic waves (see below).

b. *Sensitivity tests*

When the offshore tidal forcing is reduced by 50% (run 2), F_x, F_y, C, T, ε' (Figs. 2b–f), and E_k (Fig. 5a) are all greatly diminished (also in Table 2). Because F_x, F_y, ε', and E_k are all quadratic quantities of baroclinic variables, they would be expected to decline to a quarter of their run-1 values if the system is baroclinically linear. Figure 5c and Table 2 show that the ratio of E_k in runs 2 and 1 is around 1/4. Similar ratios are obtained for F_x and F_y. These suggest that the baroclinic M_2-generation process behaves in linear fashion, consistent with C and $-\nabla \cdot \mathbf{F}$ being the predominant terms in the energy budget. The increased nonlinearity in run 1 versus run 2 does affect development of low-energy but potentially high-shear harmonics, however, discussed in another section.

However, completely neglecting $\mathbf{u} \cdot \nabla \mathbf{u}_h$ (run 3) substantially modifies the modeled internal wave–field energy. In particular, C and E_k integrated over the area spanning 60 km across the shelf break are reduced by 33% and 27%, respectively (Table 2). The reduction of F_x on the shelf is even greater—more than 50% (Fig. 2b). There is an increase of turbulence dissipation at the critical site (Fig. 2f), but the overall dissipation around the shelf break remains similar to that in run 1 (Table 2). Note that $\mathbf{U}$ is nearly identical in runs 1 and 3, so that all the described changes are caused by variations in $\mathbf{u}'$. Examination of the run 3 fields shows that the reduction of E_k is accompanied by large phase changes of the main-beam M_2 internal tides, relative to the run 1 phases (Fig. 8b). Figure 9 shows that, in run 1, W_z and ρ' at site A in the main M_2 beam are in phase, while they are not in run 3. As C_z is the greatest in the M_2 beam (Fig. 6a), the phase change greatly reduces C (Fig. 2d) defined in (8), and thus also E_k. This demonstrates the first of our highlighted results, that phases of internal tide at the shelf break are crucial information (be they entirely

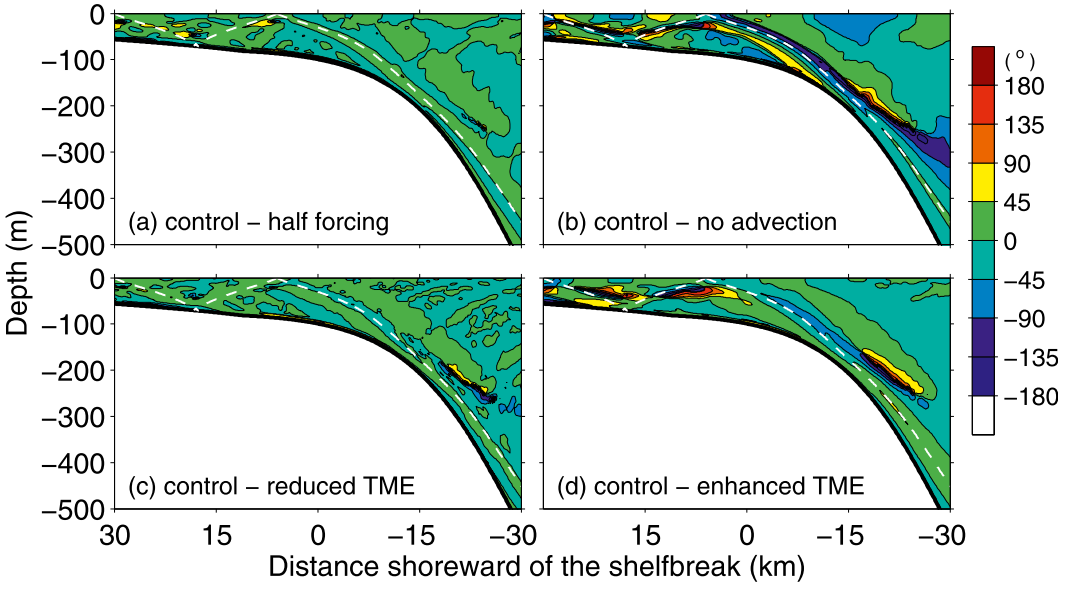

FIG. 8. Differences of the phases of internal M_2 waves between the control simulation and the simulations of (a) half forcing, (b) no advection, (c) reduced vertical TME, and (d) enhanced vertical TME. The white dashed lines represent M_2 internal-wave characteristics.

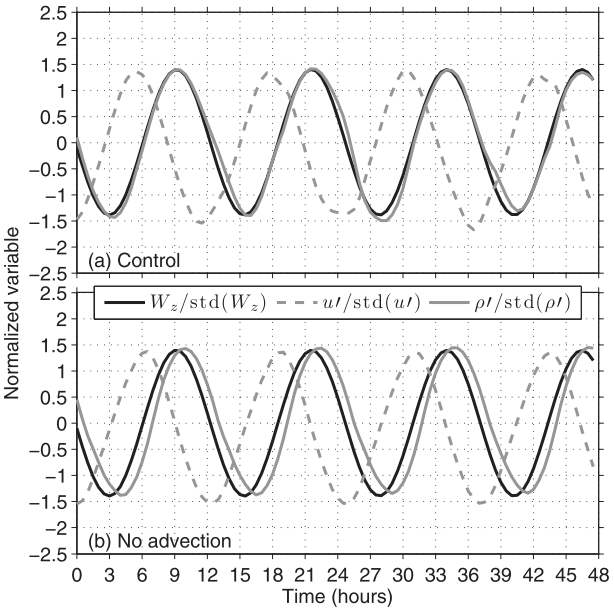

FIG. 9. Time series of normalized barotropic and baroclinic variables at site A (see Fig. 4 for its location) over days 10–11 in the (a) control (run 1) and (b) no-advection (run 3) simulations. Wave phases in the half-forcing simulation (run 2) are very similar to those in the control simulation.

locally generated, or the sum of local and incident waves), and they affect the arrival time and the energy level of internal tides on the shelf. This agrees with the findings of Kelly and Nash (2010), obtained with a simpler idealized model (see below).

Differences between runs 1, 4, and 5 quantify the noticeable influence of vertical TME on the modeled internal tides. Explicitly decreasing A_v (run 4) slightly modifies F_x (Fig. 2b) and C (Fig. 2d), greatly reduces dissipation everywhere (Fig. 2f), and magnifies the fluctuation of T (Fig. 2e). This also increases E_k everywhere (Fig. 5a), and cross-shelf-integrated E_k by 12% (Table 2)—consistent with the relative size of ε' in the energy budget of run 1. The M_2 internal-tide phase does not change much with the reduced A_v (Fig. 8c). The effects of a high A_v (run 5) are more pronounced as follows: this lowers E_k by about 53% (Table 2), with a greater reduction (about 80%) on the shelf (Fig. 5a); this also reduces F_x, C, and T (Figs. 2b–e) and essentially inhibits the onshore propagation of the baroclinic energy. The reduction of C is apparently caused by diminished $\partial \mathbf{u}'/\partial z$, reduced M_2 beam strength, and reduced ρ'. Increasing A_v also modifies the phases of the internal M_2 tide in the beam by about 45° near the shelf break and much more on the shelf (Fig. 8d). Note that, in run 5, while A_v is increased to $10^{-2}\,\mathrm{m^2\,s^{-1}}$, κ_v is reduced to $10^{-6}\,\mathrm{m^2\,s^{-1}}$, a value typically used in nonhydrostatic simulations of internal waves. Increasing A_v alone has greatly reduced E_k, we speculate that increasing both A_v and κ_v would reduce it even further.

c. Internal wave–wave interaction

Super- and subharmonic internal waves are generated in our control simulation, as shown by the power spectral densities (PSDs) of the modeled u' at sites A and B (Figs. 10a and 10b), and as found in related previous studies (e.g., Korobov and Lamb 2008; Nikurashin and Legg 2011). The PSDs are computed from velocity time series over the period of days 5–25. The expected maximum PSD at both sites is at M_2 frequency. The site A PSD contains peaks, significant at 95% confidence level, at frequencies of $M_2/2$, M_3, M_4, M_5 and M_6, whereas the site B PSD only has significant peaks at frequencies that are harmonics of M_2. Because of the absence of external disturbances, there is no peak at inertial frequency at either site.

To verify the modeled super- and subharmonic waves, PSDs were computed for velocities observed with Shallow Water '06 Experiment moorings (Newhall et al. 2007; Tang et al. 2007). Figures 10c and 10d show spectra of observed u' at depths of 458 and 126 m, respectively, during the period from 27 July 2006 to 21 September 2006 by Mooring SW43 at a site with a water depth of 480 m (see Fig. 1 for its location). The average of the spectra at all depths at the site is also given for reference. A PSD peak significant at 95% confidence level occurs near $M_2/2$ at 458 m (Fig. 10c). Note that $M_2/2$ signals and nearby O_1 tidal frequency signals are inseparable in the record. Although they cannot be proven to be $M_2/2$ waves, the observed peak near $M_2/2$ demonstrates the existence of forced and/or spatially trapped waves in the MAB shelfbreak region, as the mooring site is north of the critical latitude of both $M_2/2$ and O_1 internal waves (~29.9°). Similar forced subinertial baroclinic waves of diurnal frequency have been reported at Yermak Plateau (Fer et al. 2010; Padman et al. 1992). An additional significant peak at M_4 is found in the Mooring SW43 u' spectrum for 126-m depth (Fig. 10d). These confirm the natural occurrence of the modeled superharmonic internal waves near the shelf break. Note that the observed spectral peaks are much less evident than modeled, a possible consequence of remotely generated waves and local disturbances from various factors (e.g., winds and mesoscale activities) that are not represented in the model. The absence of these processes and of nonhydrostatic effects, along with numerical errors, might also cause the modeled spectrum to drop more rapidly versus frequency than the observed.

To examine the inhomogeneous structures of modeled internal-wave fields, u' signals at $M_2/2$, M_2, M_3, and M_4 frequencies were extracted at every grid point using

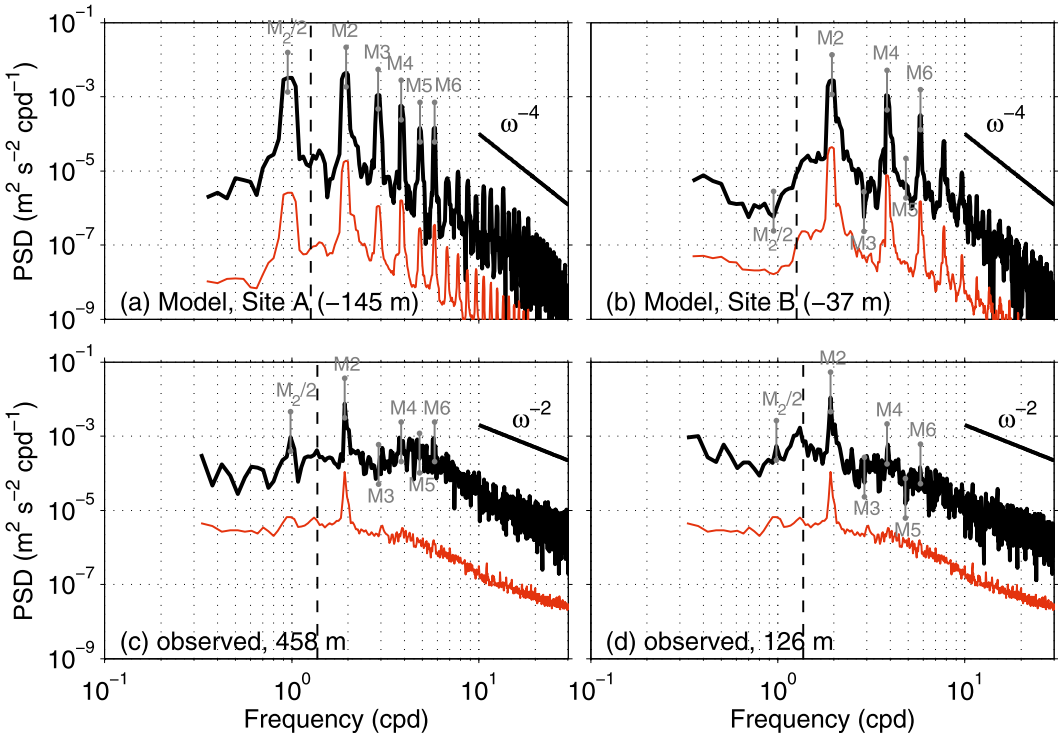

FIG. 10. PSD (black lines) of (a),(b) modeled (see Fig. 4 for the locations of sites A and B) and (c),(d) observed (see Fig. 1 for the mooring location) cross-shelf baroclinic velocity. The gray lines indicate 95% confidence intervals at selected frequencies; the dashed lines indicate the inertial frequency; the black solid straight lines indicate the slopes of −2 and −4, respectively; the red lines are the depth-averaged PSD at the same locations offset downward by a factor of 100.

harmonic demodulation. A snapshot of the M_2 velocity component at day 10 (Fig. 11b) shows a smooth M_2 beam tangent to the critical slope. The $M_2/2$ velocity (Fig. 11a) depicts an oscillatory pattern in the vertical direction, strongest in the M_2 beam, with typical vertical wavelengths of 20–30 m. Some weak $M_2/2$ signal is also visible along an M_3 beam. A hotspot of strong $M_2/2$ velocity exists approximately 4 km inshore of the critical isobath. Site A sits in the middle of the hotspot. Although $M_2/2$ motions are most intense at the hotspot, features of the $M_2/2$ waves (e.g., k_z) are similar throughout the M_2 beam. Patterns of the M_3 velocity resemble those of $M_2/2$, except that M_3 energy is less concentrated in the M_2 beam, and weak M_3 beams are visible both onshore and offshore of the hotspot (Fig. 11c). The M_4 velocity shows a beam originating at the critical slope and reflecting multiple times off the surface and bottom (Fig. 11d).

The development time scales of the super- and subharmonic waves indicate the rates of energy transfer. To quantify development, we conducted wavelet analysis on u' at sites A and B using the Morlet basis function (Torrence and Compo 1998). The results depict the gradual appearance of significant peaks at M_2, M_4, and M_6 frequencies at both sites (Fig. 12). The appearance time increases with frequency. It takes 1 and 2 days for the peaks at M_4 and M_6 frequencies to become significant, respectively. Site A results show additional significant peaks at $M_2/2$, M_3, and M_5 frequencies. The site A $M_2/2$ peak emerges at the very beginning of the simulation, while the M_3 and M_5 peaks at emerge at days 4 and 7, respectively.

To confirm that the super- and subharmonic waves are caused by nonlinear internal wave–wave interaction, bispectral methods (Kim and Powers 1979) were applied to u' at the two sites (Fig. 13). Bicoherence $\Phi(\omega_1, \omega_2)$ measures the coherency between waves at three frequencies: the primary frequency pair, ω_1 and ω_2, and the sum frequency, $\omega_3 = \omega_1 + \omega_2$. The bispectrum $\Psi(\omega_1, \omega_2)$ measures the amount of energy involved in the three-wave coupling. Each point in the bicoherence plot denotes the degree of coupling between waves at ω_1 and ω_2—which concur with the plot axes—and ω_3, with symmetric appearance about the $\omega_1 = \omega_2$ diagonal line. If a wave at ω_3 is excited by the interaction of waves at ω_1 and ω_2, or, in the case of $\omega_1 = \omega_2$, waves at ω_1 are excited by a wave at ω_3, $\Phi(\omega_1, \omega_2)$ will have a value close to 1.

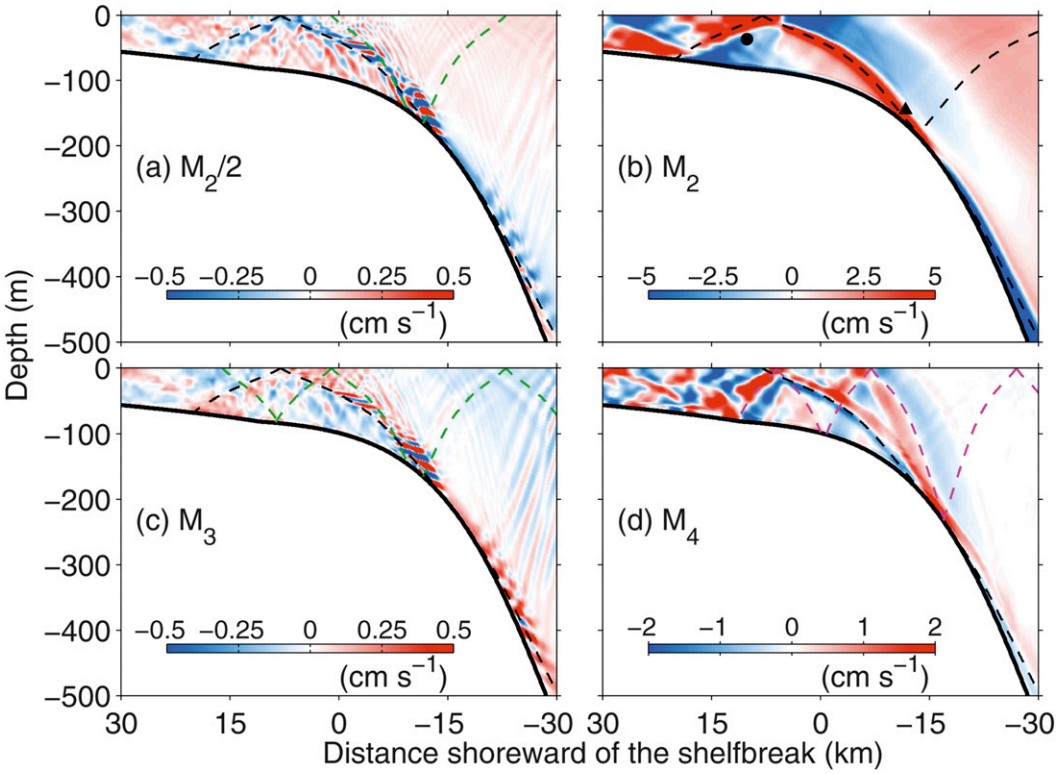

FIG. 11. Snapshots of demodulated cross-shelf baroclinic velocity at different frequencies at day 10. The triangle and circle indicate the locations of sites A and B, respectively. The dashed black, green, and magenta lines represent internal-wave characteristics at frequencies of M_2, M_3, and M_4, respectively.

The site A bicoherence (Fig. 13a) is near 1 at most of the primary frequency pairs with members of multiples of $M_2/2$ and which sum to less than M_7, for example, ($M_2/2$, $M_2/2$), ($M_2/2$, M_2), (M_2, M_2), and (M_3, M_3). This suggests interaction between waves in frequency groups ($M_2/2$, $M_2/2$, and M_2); ($M_2/2$, M_2, and M_3); (M_2, M_2, and M_4); (M_3, M_3 and M_6), etc. The bispectrum for site A (Fig. 13c) indicates that the three most energetic coupling frequency groups are as follows: (M_2, M_2, and M_4); ($M_2/2$, $M_2/2$, and M_2); and ($M_2/2$, M_2, and M_3). Coupling in other frequency groups, although measurable with statistical significance, involves very little energy. The situation at site B is simpler (Fig. 13b); the only significant bicoherence peaks are for primary pair frequencies at the harmonics of M_2 (M_2, M_4, and M_6, etc.). The corresponding bispectrum distribution (Fig. 13d) shows a consistent pattern that indicates that energetic coupling takes place only within two groups: (M_2, M_2, and M_4) and (M_2, M_4, and M_6). Minor and insignificant peaks at ($M_2/2$, $M_2/2$) and ($M_2/2$, M_2) are present, indicating that $M_2/2$ and M_3 waves of very weak intensity are generated at sites like "B" off the M_2 beam.

The wavelet and bispectral analyses confirm that nonlinear internal wave–wave interactions take place in the model near the shelfbreak internal tide–generation area, and that effects are not uniform in space, with relatively strong (initially) $M_2/2$ and (subsequently) M_3 waves appearing at site A, but not B. To further examine the spatial inhomogeneity, bispectrum cross sections at four discrete primary frequency pairs are shown in Fig. 14. Energetic wave–wave interactions take place mainly along the M_2 beam. The frequency group (M_2, M_2, and M_4) shows additional features (Fig. 14c, note that the color scaling in Fig. 14c differs from the others): relatively energetic offbeam interactions occur on the shelf, as also demonstrated by the bispectrum pattern at site B (Fig. 13).

The energy involved in the wave–wave interactions, and its spatial distribution, can be quantified. Cross sections of the demodulated E_{kz} in the control simulation (Fig. 15, the first column) show that $M_2/2$ energy is concentrated mostly in the M_2 beam, consistent with the trapping of forced subharmonic waves in a tidal beam found by Korobov and Lamb [(2008), see their Fig. 9a]. The M_3 wave (Fig. 15i) is relatively intense along the M_2 beam, and its propagation along an M_3 characteristic is also visible. The M_4 wave is distributed much more widely, and its intensity is rather high everywhere on the

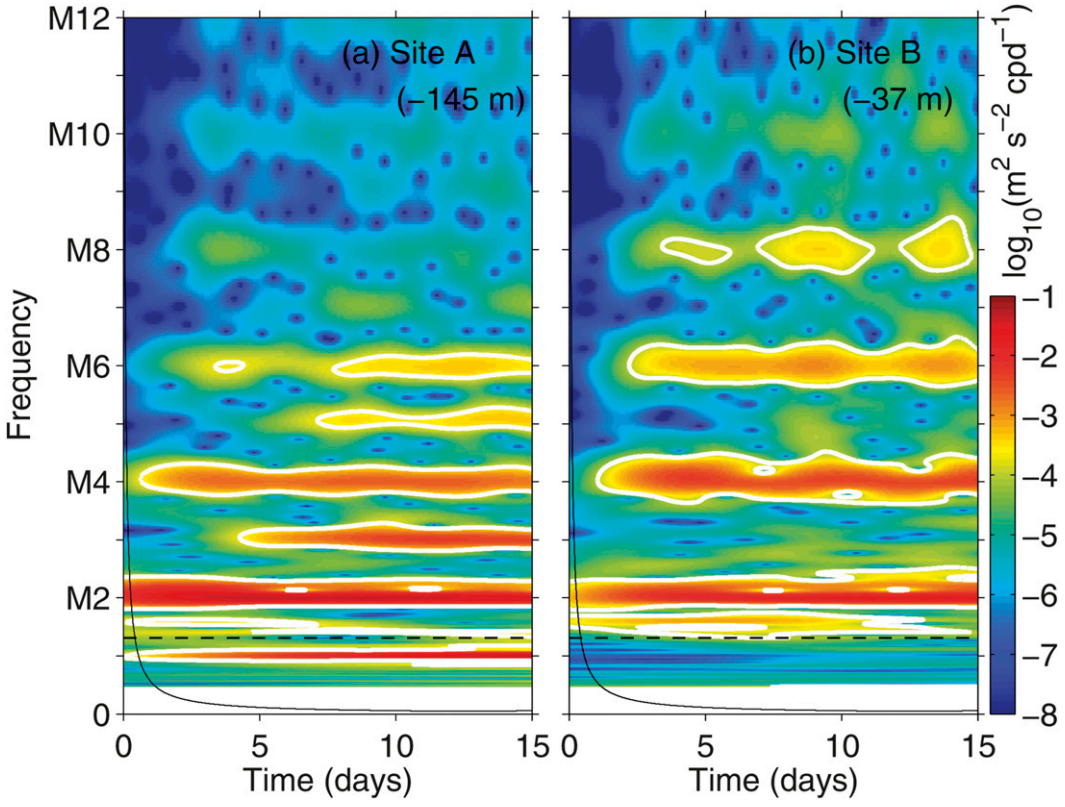

FIG. 12. The wavelet power spectra of cross-shelf baroclinic velocity at sites (a) A and (b) B in the control simulation. Locations A and B are shown in Figs. 4 and 11. The white contours outline the 95% confidence level; the dashed lines indicate the inertial frequency; and the black solid line indicates the ''cone of influence,'' where edge effects become important. Note that only the results in the first 15 days are shown.

shelf. The figure shows that the $M_2/2$ and M_3 wave energy levels are more than two orders of magnitude smaller than that of the M_2 wave in most places, while that of the M_4 wave is much higher than those of $M_2/2$ and M_3 waves, particularly on the shelf. Figure 5b shows that E_k at $M_2/2$ and M_3 are both 5% of that of M_2 at the hotspot (in the x direction) where site A lies, respectively, and there is less $M_2/2$ or M_3 energy elsewhere. The E_k at M_4 is weaker than M_2 by about one order of magnitude onshore of the shelf break and by more than two orders of magnitude offshore. These energy levels suggest that nonlinear internal wave–wave interaction drains 5%–10% of the kinetic energy from the primary M_2 wave on the shelf and near the shelf break, with a much lower fraction of M_2 energy converted in the deep sea.

Nonlinear momentum advection is the process responsible for most of the wave–wave interaction. Without it there is no internal-wave kinetic energy at frequencies $M_2/2$ and M_3, and very little energy at frequency M_4 (Fig. 15, the second column). The other nonlinear processes in the system, namely the vertical mixing parameterizations for momentum and scalars and the nonlinear equation of state, are responsible for the residual run 3 M_4 waves. This was confirmed with a test simulation having minimum vertical TME and mixing and a linear equation of state (results not shown). Reducing the viscosity and diffusivity to near molecular values (run 4) increases the internal-wave kinetic energy slightly above run 1 levels in the super- and subharmonic frequencies (Fig. 15, the third column). Increasing vertical viscosity to $10^{-2}\,\mathrm{m^2\,s^{-1}}$ (run 5) suppresses almost all the internal-wave kinetic energy at $M_2/2$ and M_3 frequencies and reduces M_4 energy substantially. The run-5 findings have important implications for internal-wave modeling and are discussed in section 4.

4. Discussion

a. *Effects of nonlinear advection*

The energy budget calculation (section 3) suggests that nonlinear momentum advection is not a major source of internal-tide energy in the shelfbreak region

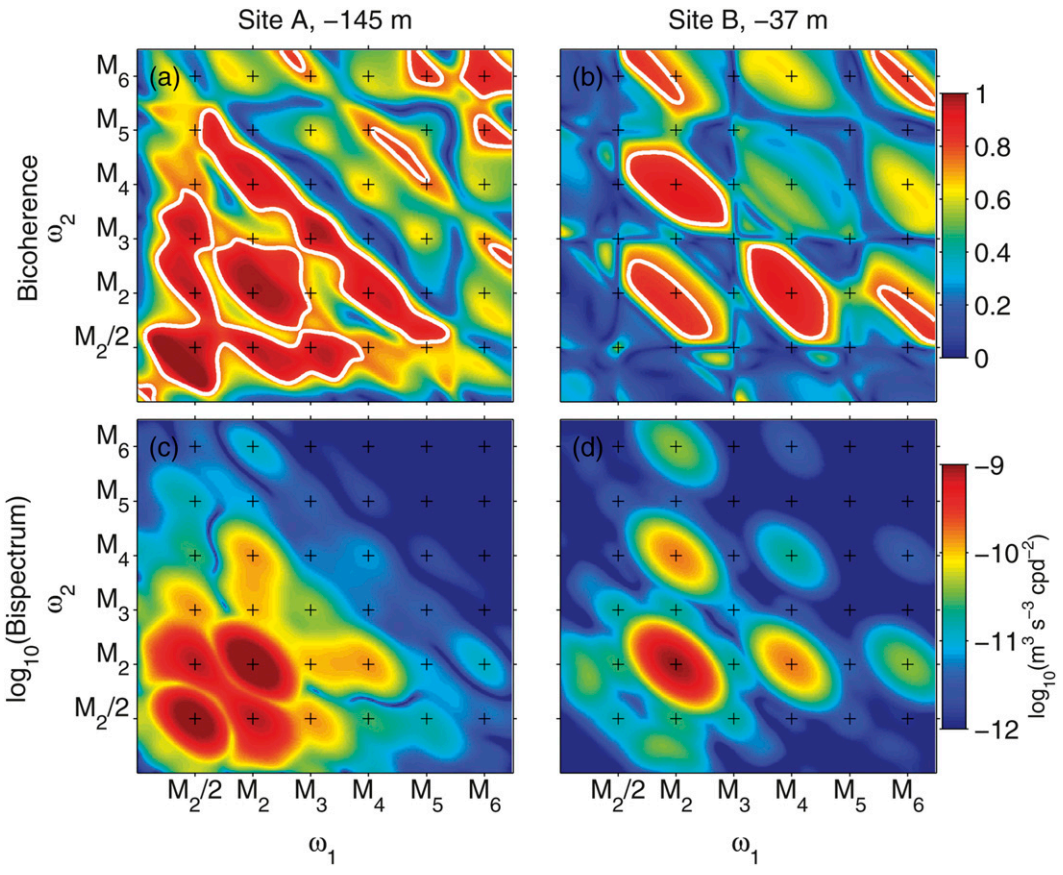

FIG. 13. (a),(b) Bicoherences and (c),(d) bispectra computed from cross-shelf baroclinic velocity at sites A (left) and B (right) in the control simulation. Locations A and B are shown in Figs. 4 and 11. The white contours outline the 95% confidence level of the bicoherence.

(Table 2 and Fig. 7). Nevertheless, $\mathbf{u} \cdot \nabla \mathbf{u}_h$ exerts strong influences on the internal-tide generation, evident from its effect on the internal-tide phase (Figs. 8b and 9) and energy level (thus also the generation efficiency, if one compares runs 1 and 3 sharing common forcing). Comparing runs 1 and 3 indicates that deleting $\mathbf{u} \cdot \nabla \mathbf{u}_h$ reduces E_k (Fig. 5a), F_x, and C (Fig. 2) by roughly 30% each. Advection of the internal tide by the background flow $\mathbf{U}$ is the main mechanism at work. The wavelength of $\mathbf{U}$ is much larger than that of $\mathbf{u}'$, and the relative phase of the two is a strong function of x, giving a strong spatial dependence to this term and the total tidal flow field. The effect of phase is illustrated by the study of Kelly and Nash (2010), whereby an internal-tide incident on a slope can strongly affect baroclinic tidal conversion at the slope. The total currents at the seabed are linked to the efficacy of the conversion process; cancellation of barotropic and baroclinic currents there diminishes the potential energy oscillations created at the sloping seabed and thus the baroclinic wave generation. Also, W_z and ρ' being in quadrature would give no net generation. Note that the energy budget calculation does not divulge the effect of phase. Also note that disregarding advection does not necessarily reduce internal-tide energy as in this example.

The findings also discourage the use of linear internal tide–generation theory at supercritical slopes such as at the MAB shelf break. The linear internal-wave theory (Bell 1975; Pétrélis et al. 2006) is based on a weak topography approximation, and is valid only when $\gamma \ll 1$, $\delta \ll 1$, and $\gamma R \ll 1$ (Balmforth et al. 2002; Garrett and Kunze 2007). Because the steep slope offshore of the shelf break makes $\gamma > 1$ and $\delta \approx 0.9$, it is not surprising for nonlinearity to play a role there. Garrett and Kunze (2007) presumed that the breakdown of the linear assumption in the case of steep topography in deep sea does not affect the overall baroclinic energy flux because the energy flux is mostly carried out by large-scale internal-wave motions and the nonlinearity is mainly associated with small-scale waves. The order-twofold increase of baroclinic energy flux on the shelf from quasi-linear to nonlinear models obtained here argues

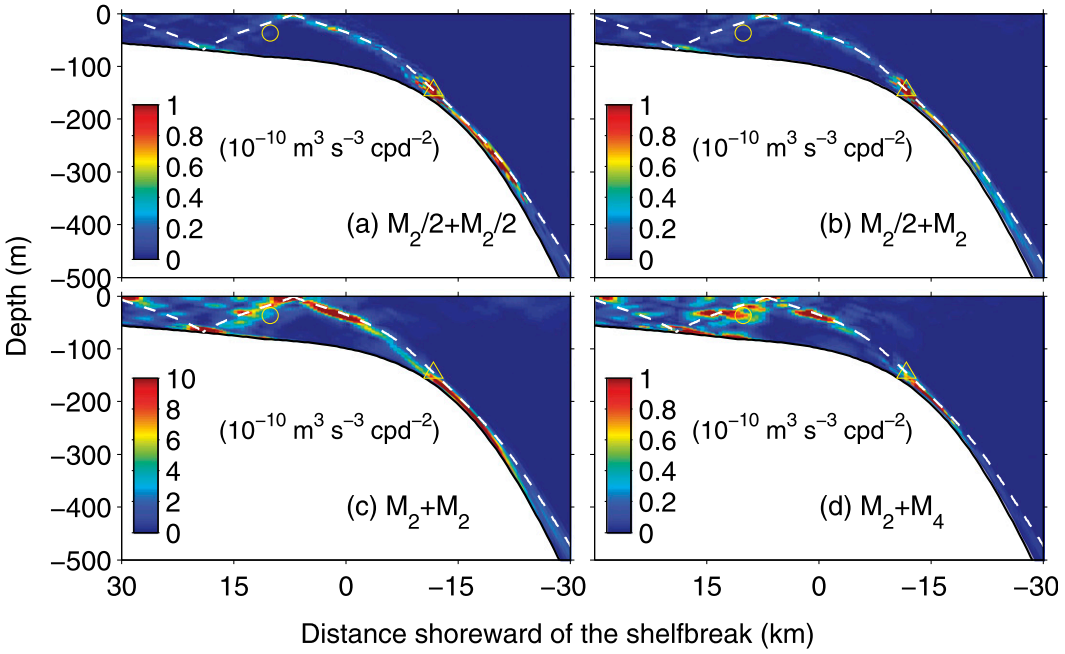

FIG. 14. Cross-shelf sections of bispectra of different frequency pairs computed from cross-shelf baroclinic velocity in the control simulation. The triangles and circles indicate the locations of sites A and B, respectively. The white dashed lines represent M_2 internal-wave characteristics.

against making this presumption regarding the onshore radiation of shelfbreak-generated internal tides.

Another difference between runs 1 and 3 resides in the super- and subharmonic waves (Fig. 15). The lack of harmonics with no advection implies that the waves are generated by $\mathbf{u} \cdot \nabla \mathbf{u}_h$, which is confirmed by the diminished relative harmonic formation in run 2 (Fig. 5c). The $\nabla \mathbf{U}_h$ is very small, so $\mathbf{u} \cdot \nabla \mathbf{u}'_h$ is the main term. Overall, nonlinear advection converts 5%–10% of the total run-1 internal-wave kinetic energy to internal waves at $M_2/2$, M_3, and M_4 frequencies, a small fraction, but possibly important for local TME, particularly within the M_2 beam (Fig. 16). We will discuss the non-M_2 waves in more detail in the sections to follow.

b. *Effects of vertical TME*

Internal waves are believed to be major sources of mixing in the ocean (Munk and Wunsch 1998), and quantifying ocean mixing triggered by internal waves has been a major objective of many studies (e.g., Green et al. 2008; Lien and Gregg 2001; Nash et al. 2007). The comparison between runs 1 and 4 suggests that the GLS turbulence closure in the model dissipates about 14% of the internal-wave kinetic energy (Fig. 5a). This suggests that internal-wave kinetic energy near the shelf break, and radiating away, may be overestimated if vertical TME is neglected, a simplification that is often used along with the assumption of linearity (e.g., Pétrélis et al. 2006).

On the other hand, with elevated A_v, internal-wave energy may be underestimated greatly, especially on the shelf. Comparison between runs 1 and 5 indicates that a substantial portion of the internal-wave kinetic energy is damped by the high viscosity, from 50% at the shelf break (Table 2) to even more on the shelf (Fig. 5a). Because internal-wave simulations with primitive equation models sometimes utilize high vertical momentum viscosity values from 10^{-3} to $10^{-1}\,\mathrm{m^2\,s^{-1}}$ (e.g., Green et al. 2008; Nash et al. 2012), caution is needed when interpreting the results on continental shelves. Another consequence of the elevated A_v is the complete disappearance of the $M_2/2$ and M_3 waves and substantial suppression of the M_4 waves (Fig. 15). Because the vertical scale of the subharmonic waves is much smaller than that of the primary M_2 waves, they have high shear and are more vulnerable to damping by eddy viscosity. This may explain why subharmonic internal waves are not prominent in some of the previous simulations.

The hydrostatic model cannot resolve small-scale processes of TME and mixing and substitutes a subgrid mixing parameterization. The quantifications made here about effects of vertical TME may depend on the turbulence closure scheme, and therefore might not be definitive measures of the interactions between internal waves and TME in the modeled scenario. However, we postulate that the qualitative results are valid. That is, internal waves and turbulence processes are very much

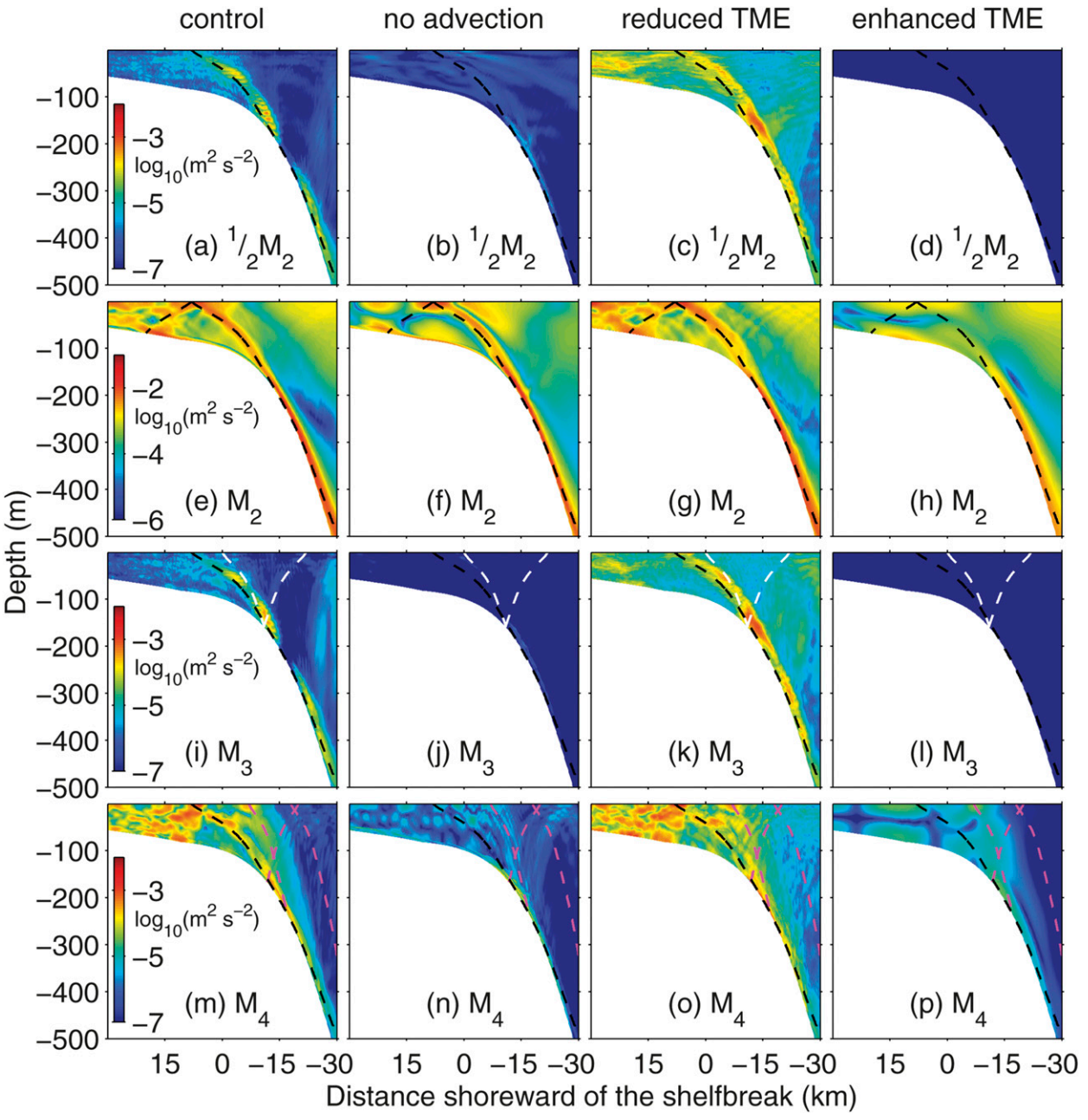

FIG. 15. Cross-shelf sections of the internal wave kinetic energy at different frequencies in simulations of different physics. (a) The dashed-black, white, and magenta lines represent internal-wave characteristics at frequencies of M_2, M_3, and M_4, respectively. Each color bar is for panels in the entire row.

coupled, and any attempt to separate them may cause errors in quantitative estimates for each processes. Unfortunately, the coupling between internal waves and turbulence involves processes over a broad range of scales, from tens of kilometers (the scale of internal tides) to decimeters (the scale of Kelvin–Helmholtz instability); this multiscale coupling makes simulation of tidally controlled internal waves challenging.

c. *Effects of wave–wave interaction*

The creation of internal waves at harmonic overtones ($\omega = n\omega_0$, where ω_0 is the forcing frequency and $n = 2, 3, \ldots$) through nonlinear wave–wave interaction near an internal tide–generation site has been documented in different slope and excursion parameter regimes: 1) $\gamma < 1$ and $R > 1$ (Bell 1975), 2) $\gamma < 1$ and $R < 1$ (Legg and

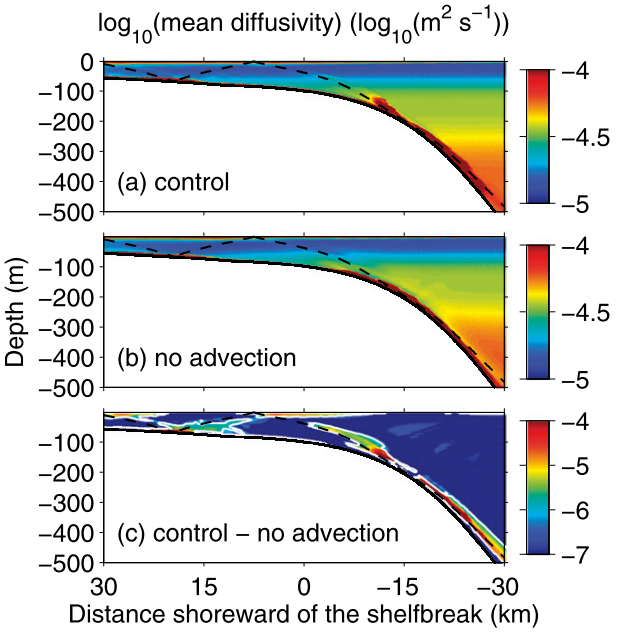

FIG. 16. Cross-shelf sections of the mean diffusivity in the (a) control and (b) no-advection simulations and (c) the differences between them. The white contours in (c) outline the difference of $10^{-6}\,m^2\,s^{-1}$. The black dashed lines represent M_2 internal-wave characteristics.

Huijts 2006), 3) $\gamma > 1$ and $R < 1$ (Gayen and Sarkar 2011; King et al. 2010; Korobov and Lamb 2008; Lamb 2004; Legg and Huijts 2006; Sun and Pinkel 2012), and 4) $\gamma > 1$ and $R \geq 1$ (King et al. 2010; Legg and Huijts 2006). This MAB shelfbreak M_2 study falls into the third category. Our simulations suggest that wave–wave interaction acts in this process with a time scale of from one to two M_2 forcing periods (Fig. 12).

The modeled $M_2/2$ waves in the main M_2 beam are intriguing. Generation of subharmonic features of this type is usually studied at latitudes near or below the critical latitude where $\omega = 2f$ (~28.8° for M_2 frequency), and where PSI is considered to be the primary mechanism (Carter and Gregg 2006; Gerkema et al. 2006; Lamb 2004; MacKinnon and Winters 2005). The specified rotation corresponds to the latitude of 39°, and $\omega_{M_2}/2 \approx 0.765f$. It is widely believed that PSI does not occur when $\omega_0/2 < f$. However, Korobov and Lamb (2008) demonstrated the generation of forced subinertial $M_2/2$ waves by M_2 motions. By squaring (17) with $N > f$ it can be deduced that at least one of the subinertial wavenumber components k_x or k_z must be complex, and that the waves are not free and must decay exponentially in some direction. Consistent with the finding of Korobov and Lamb, the MAB simulation $M_2/2$ oscillations are concentrated in the main M_2 beam, which suggests that the beam is a source region around which the nonlinear advection is the strongest (Fig. 6b) and the generated $M_2/2$ waves are trapped.

Departing from the perception that PSI only occurs via weakly nonlinear resonant interactions, Korobov and Lamb attributed the $M_2/2$ waves to PSI associated with nonresonant triad interactions in a regime of strong nonlinearity. That is, PSI passes energy from the primary frequency to lower frequencies (here, forced $M_2/2$) with weak or nonexistent return (resonant) transfer. Although details of the physical process are unclear, the interactions between $M_2/2$ and M_2 waves are confirmed by our bispectrum analysis. In the field, Carter and Gregg (2006) observed strong $M_2/2$ motions in an M_2 internal-wave beam near Hawai'i and suggested nonresonant strong nonlinear interaction as a possible explanation. Nonresonant nonlinear interaction is also believed to be the cause of superharmonic beams generated in numerical (Lamb 2004) and laboratory (Teoh et al. 1997) internal-wave studies. Interestingly, the nonlinear interaction in Teoh et al. (1997) caused evanescent waves at frequencies $\omega > N$, also outside the internal wave band, and trapped at the intersection of two internal-wave beams, where they were generated, similar to the $M_2/2$ waves shown here.

The $M_2/2$ waves are generated not only from M_2 waves alone through PSI but also from nonlinear interactions between M_2 and M_3 waves. The weak $M_2/2$ signal along M_3 beams is evidence of this (Fig. 11a). The M_3 waves generated in the M_2 beam through nonlinear interactions propagate away from the source region. These waves then interact with M_2 waves, generating $M_2/2$ off the M_2 beam. These off-beam interactions between M_2 and M_3 waves involve little energy, and it is unlikely that they would be observable in nature.

The strong vertical shear associated with the energetic large-k_z beam-trapped $M_2/2$ motions contributes significant vertical TME, as suggested by the resemblance between the patchy pattern of energy dissipation (Fig. 6d) and $M_2/2$ wave field (Fig. 11a). Run 3, with no $M_2/2$ waves, has lower diffusivity (Fig. 16). The significant run 1 TME is consistent with enhanced TME from simulated subharmonic free waves (Hazewinkel and Winters 2011). Enhanced shear of trapped $M_2/2$ waves might (speculatively) partially explain observed strong turbulence along an M_2 internal tidal beam near the shelf break to the east of Monterey Bay (Lien and Gregg 2001).

5. Summary

This study investigates the generation of internal tides and the associated internal wave–wave interactions in a continental shelfbreak region using a hydrostatic model.

An idealized configuration that mimics the Mid-Atlantic Bight shelf break is used. The model simulations are forced with an oscillating tidal current of M_2 frequency at the offshore boundary, and the system falls into the category of supercritical slope, low excursion, and Froude numbers. The control simulation (run 1) produces internal tides with an integrated barotropic-to-baroclinic conversion rate of about 335 $W m^{-1}$ in a zone of 60 km across the shelf break. About 14% of internal-tide energy ($\sim$46.5 $W m^{-1}$) is dissipated locally through turbulence and bottom dissipation, 18% ($\sim$60 $W m^{-1}$) radiates onshore, and the remaining radiates offshore. Additional simulations are performed to examine processes in greater detail.

Spectra of internal waves generated within the nonlinear control simulation show discrete and significant peaks at frequencies of $M_2/2$, M_2, M_3, M_4, and so on. Spectra of produced internal waves vary strongly in space, with two sites examined in detail, one within a narrow beam of strong M_2 internal-wave energy and one outside of the beam. Bispectrum analysis confirms that the super- and subharmonic waves are generated by nonlinear internal wave–wave interactions mostly through the nonlinear baroclinic advection in the momentum equations, as verified by reducing tidal forcing and by ''turning off'' advection in two separate simulations. The nonlinear wave–wave interactions are the most intensive within a beam where M_2 internal waves are the strongest. Consistent with the study of Korobov and Lamb (2008) on the topic in a similar environment, the unusual $M_2/2$ waves appear predominantly in the beam as trapped waves. It is believed that the subinertial $M_2/2$ waves are generated through nonresonant triad interaction in the M_2 beam where nonlinearity is strong.

The role of nonlinear effects was quantified by looking at other features of the modeled internal waves. Comparisons between simulations with and without momentum advection indicate that nonlinear effects enhance cross-shelf baroclinic flux, barotropic-to-baroclinic energy conversion rate, and internal-wave kinetic energy, all by about 30% near the shelf break and even more on the shelf. However, energy analyses of the control simulation indicate that nonlinear momentum advection is not a direct source of internal tides at the shelf break. Rather, it modifies phases of the M_2 internal tides and thus the efficiency of barotropic-to-baroclinic conversion. This implies that linear internal wave–generation theory has limited utility at supercritical slope shelfbreak conditions, with phases and amplitudes of continental shelf internal tides linked to nonlinearity. It also exposes the limitation of energy budget calculations in diagnosing the contributions of specific internal tide–generation processes.

The model also suggests that vertical turbulent momentum exchange (TME) is important in controlling the internal waves at the shelf break. With general length scale turbulence closure, the model converts about 14% of the internal-wave kinetic energy to local TME. Although the optimality of this turbulence closure scheme is unproven, the conclusion here—that neglecting TME causes nontrivial overestimate of the internal-wave energy at the shelf break—is very likely to be true. A consistent finding is that significant enhancement of vertical eddy viscosity, as sometimes used in internal-wave modeling for computational reasons, substantially suppresses the internal-wave activity. The results here imply that internal waves and local TME in the boundary zone are very much coupled, and they need to be considered simultaneously for a complete understanding of internal wave–energy budgets and generation processes. This agrees with the philosophy behind recent works involving unified internal-wave generation and dissipation, including those forced by tides (Klymak and Legg 2010; Klymak et al. 2010).

The subject of shelf-edge internal-wave generation and transformation is a small part of the large problem of internal wave energy balance in the ocean. Because the shelf break is a conduit in the transport of internal-wave energy between coastal and open oceans, and because, as demonstrated in this and numerous other studies, it is a source of internal waves, processes in shelfbreak regions can affect the internal-wave fields in both coastal and deep seas. Finally, the results achieved here concerning internal tides are for a single idealized scenario in the vast shelfbreak parameter space that includes spatially and temporally varying stratification, many types of topography, and many external (nontidal) influences. Further studies of all these factors would be needed to obtain a more thorough understanding of internal-wave dynamics at the shelf edge and beyond.

Acknowledgments. We thank Drs. Steven Jachec, Kevin Lamb, Ying-Tsong Lin, James Lynch, Matthew Paoletti, Oliver Sun, Harry Swinney, John Wilkin, and Likun Zhang for useful discussions during the course of the study. This research was supported by Office of Naval Research Grant N00014-11-1-0701.

REFERENCES

Apel, J. R., and Coauthors, 1997: An overview of the 1995 SWARM shallow-water internal wave acoustic scattering experiment. *IEEE J. Oceanic Eng.,* **22,** 465–500.

Balmforth, N. J., G. R. Ierley, and W. R. Young, 2002: Tidal conversion of subcritical topography. *J. Phys. Oceanogr.,* **32,** 2900–2914.

Bell, T. H., 1975: Topographically generated internal waves in the open ocean. *J. Geophys. Res.,* **80,** 320–327.

Carter, G. S., and M. C. Gregg, 2006: Persistent near-diurnal internal waves observed above a site of M_2 barotropic-to-baroclinic conversion. *J. Phys. Oceanogr.,* **36,** 1136–1147.

Chapman, D. C., 1985: Numerical treatment of cross-shelf open boundaries in a barotropic ocean model. *J. Phys. Oceanogr.,* **15,** 1060–1075.

Eckmann, J.-P., and D. Ruelle, 1985: Ergodic theory of chaos and strange attractors. *Rev. Mod. Phys.,* **57,** 617–656.

Fer, I., R. Skogseth, and F. Geyer, 2010: Internal waves and mixing in the Marginal Ice Zone near the Yermak Plateau. *J. Phys. Oceanogr.,* **40,** 1613–1630.

Flather, R. A., 1976: A tidal model of the northwest European continental shelf. *Mem. Soc. Roy. Sci. Liege,* **10,** 141–164.

Garrett, C., and E. Kunze, 2007: Internal tide generation in the deep ocean. *Annu. Rev. Fluid Mech.,* **39,** 57–87, doi:10.1146/annurev.fluid.39.050905.110227.

Gayen, B., and S. Sarkar, 2011: Direct and large-eddy simulations of internal tide generation at a near-critical slope. *J. Fluid Mech.,* **681,** 48–79, doi:10.1017/jfm.2011.170.

Gerkema, T., C. Staquet, and P. Bouruet-Aubertot, 2006: Decay of semi-diurnal internal-tide beams due to subharmonic resonance. *Geophys. Res. Lett.,* **33,** L08604, doi:10.1029/2005GL025105.

Green, J. A. M., J. H. Simpson, S. Legg, and M. R. Palmer, 2008: Internal waves, baroclinic energy fluxes and mixing at the European shelf edge. *Cont. Shelf Res.,* **28,** 937–950, doi:10.1016/j.csr.2008.01.014.

Hazewinkel, J., and K. B. Winters, 2011: PSI of the internal tide on a beta Plane: Flux divergence and near-inertial wave propagation. *J. Phys. Oceanogr.,* **41,** 1673–1682.

Holloway, P. E., and B. Barnes, 1998: A numerical investigation into the bottom boundary layer flow and vertical structure of internal waves on a continental slope. *Cont. Shelf Res.,* **18,** 31–65.

——, P. G. Chatwin, and P. Craig, 2001: Internal tide observations from the Australian northwest shelf in summer 1995. *J. Phys. Oceanogr.,* **31,** 1182–1199.

Javam, A., J. Imberger, and S. W. Armfield, 1999: Numerical study of internal wave reflection from a sloping boundaries. *J. Fluid Mech.,* **396,** 183–201.

——, ——, and ——, 2000: Numerical study of internal wave–wave interactions in a stratified fluid. *J. Fluid Mech.,* **415,** 65–87.

Kang, D., and O. Fringer, 2012: Energetics of barotropic and baroclinic tides in the Monterey Bay area. *J. Phys. Oceanogr.,* **42,** 272–290.

Kantha, L. H., and C. A. Clayson, 1994: An improved mixed layer model for geophysical applications. *J. Geophys. Res.,* **99,** 25 235–25 266.

Kelly, S. M., and J. D. Nash, 2010: Internal-tide generation and destruction by shoaling internal tides. *Geophys. Res. Lett.,* **37,** L23611, doi:10.1029/2010GL045598.

Kim, Y. C., and E. J. Powers, 1979: Digital bispectral analysis and its applications to nonlinear wave interactions. *IEEE Trans. Plasma Sci.,* **PS-7,** 120–131.

King, B., H. P. Zhang, and H. L. Swinney, 2010: Tidal flow over three-dimensional topography generates out-of-forcing-plane harmonics. *Geophys. Res. Lett.,* **37,** L14606, doi:10.1029/2010GL043221.

Klymak, J. M., and S. M. Legg, 2010: A simple mixing scheme for models that resolve breaking internal waves. *Ocean Modell.,* **33,** 224–234, doi:10.1016/j.ocemod.2010.02.005.

——, ——, and R. Pinkel, 2010: A simple parameterization of turbulent tidal mixing near supercritical topography. *J. Phys. Oceanogr.,* **40,** 2059–2074.

Korobov, A. S., and K. G. Lamb, 2008: Interharmonics in internal gravity waves generated by tide-topography interaction. *J. Fluid Mech.,* **611,** 61–95, doi:10.1017/S0022112008002449.

Krishnamurthy, V., 1993: A predictability study of Lorenz's 28-variable model as a dynamical system. *J. Atmos. Sci.,* **50,** 2215–2229.

Lamb, K. G., 2004: Nonlinear interaction among internal wave beams generated by tidal flow over supercritical topography. *Geophys. Res. Lett.,* **31,** L09313, doi:10.1029/2003GL019393.

Legg, S., 2004: Internal tides generated on a corrugated continental slope. Part I: Cross-slope barotropic forcing. *J. Phys. Oceanogr.,* **34,** 156–173.

——, and A. Adcroft, 2003: Internal wave breaking at concave and convex continental slopes. *J. Phys. Oceanogr.,* **33,** 2224–2246.

——, and K. M. H. Huijts, 2006: Preliminary simulations of internal waves and mixing generated by finite amplitude tidal flow over isolated topography. *Deep-Sea Res. II,* **53,** 140–156, doi:10.1016/j.dsr2.2005.09.014.

——, and J. Klymak, 2008: Internal hydraulic jumps and overturning generated by tidal flow over a tall steep ridge. *J. Phys. Oceanogr.,* **38,** 1949–1964.

Levine, M., and T. Boyd, 2006: Tidally forced internal waves and overturns observed on a slope: Results from HOME. *J. Phys. Oceanogr.,* **36,** 1184–1201.

Lien, R.-C., and M. C. Gregg, 2001: Observations of turbulence in a tidal beam and across a coastal ridge. *J. Geophys. Res.,* **106,** 4575–4591.

Lvov, Y. V., K. L. Polzin, and N. Yokoyama, 2012: Resonant and near-resonant internal wave interactions. *J. Phys. Oceanogr.,* **42,** 669–691.

Lynch, J. F., Y.-T. Lin, T. F. Duda, and A. E. Newhall, 2010: Acoustic ducting, reflection, refraction, and dispersion by curved nonlinear internal waves in shallow water. *IEEE J. Oceanic Eng.,* **35,** 12–27, doi:10.1109/JOE.2009.2038512.

MacKinnon, J. A., and M. C. Gregg, 2005: Spring mixing: Turbulence and internal waves during restratification on the New England shelf. *J. Phys. Oceanogr.,* **35,** 2425–2443.

——, and K. B. Winters, 2005: Subtropical catastrophe: Significant loss of low-mode tidal energy at 28.9°. *Geophys. Res. Lett.,* **32,** L15605, doi:10.1029/2005GL023376.

——, M. H. Alford, O. Sun, R. Pinkel, Z. Zhao, and J. Klymak, 2013: Parametric subharmonic instability of the internal tide at 29°N. *J. Phys. Oceanogr.,* **43,** 17–28.

McComas, C. H., and F. P. Bretherton, 1977: Resonant interaction of oceanic internal waves. *J. Geophys. Res.,* **82,** 1397–1412.

Müller, P., G. Holloway, F. Henyey, and N. Pomphrey, 1986: Nonlinear interactions among internal gravity waves. *Rev. Geophys.,* **24,** 493–536.

Munk, W., and C. Wunsch, 1998: Abyssal recipes II: Energetics of tidal and wind mixing. *Deep-Sea Res. I,* **45,** 1977–2010.

Nash, J. D., E. Kunze, J. M. Toole, and R. W. Schmitt, 2004: Internal tide reflection and turbulent mixing on the continental slope. *J. Phys. Oceanogr.,* **34,** 1117–1134.

——, M. H. Alford, E. Kunze, K. Martini, and S. Kelly, 2007: Hotspots of deep ocean mixing on the Oregon continental slope. *Geophys. Res. Lett.,* **34,** L01605, doi:10.1029/2006GL028170.

——, S. M. Kelly, E. L. Shroyer, J. N. Moum, and T. F. Duda, 2012: The unpredictable nature of internal tides on continental shelves. *J. Phys. Oceanogr.,* **42,** 1981–2000.

Newhall, A. E., and Coauthors, 2007: Acoustic and oceanographic observations and configuration information for the WHOI moorings from the SW06 experiment. Woods Hole Oceanographic Institution Tech. Rep. WHOI-2007-04, 116 pp.

Nikurashin, M., and S. Legg, 2011: A mechanism for local dissipation of internal tides generated at rough topography. *J. Phys. Oceanogr.,* **41,** 378–395.

Orlanski, I., 1976: A simple boundary condition for unbounded hyperbolic flows. *J. Comput. Phys.,* **21,** 251–269.

Padman, L., A. J. Plueddemann, R. D. Muench, and R. Pinkel, 1992: Diurnal tides near the Yermak Plateau. *J. Geophys. Res.,* **97,** 12 639–12 652.

Pétrélis, F., S. G. Llewellyn Smith, and W. R. Young, 2006: Tidal conversion at a submarine ridge. *J. Phys. Oceanogr.,* **36,** 1053–1071.

Polzin, K., 2004a: A heuristic description of internal wave dynamics. *J. Phys. Oceanogr.,* **34,** 214–230.

——, 2004b: Idealized solutions for the energy balance of the finescale internal wave field. *J. Phys. Oceanogr.,* **34,** 231–246.

Rayson, M. D., G. N. Ivey, N. L. Jones, M. J. Meulencers, and G. W. Wake, 2011: Internal tide dynamics in a topographically complex region: Browse Basin, Australian North West Shelf. *J. Geophys. Res.,* **116,** C01016, doi:10.1029/2009JC005881.

Sandstrom, H., and J. A. Elliott, 1984: Internal tide and solitons on the Scotian Shelf: A nutrient pump at work. *J. Geophys. Res.,* **89,** 6415–6426.

Shchepetkin, A. F., and J. C. McWilliams, 2005: The regional oceanic modeling system (ROMS): A split-explicit, free-surface, topography-following-coordinate oceanic model. *Ocean Modell.,* **9,** 347–404.

——, and ——, 2008: Computational kernel algorithms for fine-scale, multiprocess, long-term oceanic simulations. *Handbook of Numerical Analysis. XIV: Computational Methods for the Atmosphere and the Oceans,* P. G. Ciarlet, R. Temam, and J. Tribbia, Eds., Elsevier Science, 121–183.

Shroyer, E. L., J. N. Moum, and J. D. Nash, 2010a: Energy transformations and dissipation of nonlinear internal waves over New Jersey's continental shelf. *Nonlinear Processes Geophys.,* **17,** 345–360, doi:10.5194/npg-17-345-2010.

——, ——, and ——, 2010b: Vertical heat flux and lateral mass transport in nonlinear internal waves. *Geophys. Res. Lett.,* **37,** L08601, doi:10.1029/2010GL042715.

——, ——, and ——, 2011: Nonlinear internal waves over New Jersey's continental shelf. *J. Geophys. Res.,* **116,** C03022, doi:10.1029/2010JC006332.

Sun, O. M., and R. Pinkel, 2012: Energy transfer from high-shear, low-frequency internal waves to high-frequency waves near Kaena Ridge, Hawaii. *J. Phys. Oceanogr.,* **42,** 1524–1547.

——, and ——, 2013: Subharmonic energy transfer from the semidiurnal internal tide to near-diurnal motions over Kaena Ridge, Hawaii. *J. Phys. Oceanogr.,* **43,** 766–789.

Tang, D., and Coauthors, 2007: Shallow Water '06: A joint acoustic propagation /nonlinear internal wave physics experiment. *Oceanography,* **20,** 156–167.

Teoh, S. G., G. N. Ivey, and J. Imberger, 1997: Laboratory study of the interaction between two internal wave rays. *J. Fluid Mech.,* **336,** 91–122.

Torrence, C., and G. P. Compo, 1998: A practical guide to wavelet analysis. *Bull. Amer. Meteor. Soc.,* **79,** 61–78.

Umlauf, L., and H. Burchard, 2003: A generic length-scale equation for geophysical turbulence models. *J. Mar. Res.,* **61,** 235–265.

Warner, J. C., C. R. Sherwood, H. G. Arango, and R. P. Signell, 2005: Performance of four turbulence closure models implemented using a generic length scale method. *Ocean Modell.,* **8,** 81–113.

Winters, K. B., and E. A. D'Asaro, 1997: Direct simulation of internal wave energy transfer. *J. Phys. Oceanogr.,* **27,** 1937–1945.

Young, W. R., Y. K. Tsang, and N. J. Balmforth, 2008: Near-inertial parametric subharmonic instability. *J. Fluid Mech.,* **607,** 25–49, doi:10.1017/S0022112008001742.

Zhang, W. G., G. G. Gawarkiewicz, D. J. McGillicuddy, and J. L. Wilkin, 2011: Climatological mean circulation at the New England shelf break. *J. Phys. Oceanogr.,* **41,** 1874–1893.